



NTNU – Trondheim
Norwegian University of
Science and Technology

Free Convection Model Development for the Thermal Analysis of Cavities in Subsea Christmas Trees

Silje Kalleklev Velure

Master of Science in Engineering and ICT

Submission date: July 2014

Supervisor: Stein Tore Johansen, EPT

Co-supervisor: Emad Gharaibah, GE Oil & Gas

Norwegian University of Science and Technology
Department of Energy and Process Engineering

NORWEGIAN UNIVERSITY OF SCIENCE AND TECHNOLOGY

FACULTY OF ENGINEERING SCIENCE AND TECHNOLOGY
DEPARTMENT OF ENERGY AND PROCESS ENGINEERING

Free Convection Model Development for the Thermal Analysis of Cavities in Subsea Christmas Trees

Author:

Silje K. VELURE

Supervisor NTNU:

Prof. Stein Tore JOHANSEN

Supervisor GE Oil & Gas:

Emad GHARAIBAH

Trondheim, June 2014



NTNU – Trondheim
Norwegian University of
Science and Technology



GE Oil & Gas

EPT- M-2014-124

MASTER THESIS

for

Silje Kalleklev Velure

Spring 2014

Free Convection Model Development for the Thermal Analysis of Cavities in Subsea Christmas
Trees*Modellutvikling og termisk analyse av fri konveksjon i hulrom i subsea juletrær***Background and objective**

The heat transfer and thermal analysis of subsea components (e.g. Xmas Tree) for calculating temperature distribution and investigating the cool down behaviors of the subsea components is normally based on assumptions and simplifications to reduce the analysis effort involved in the process of the computation grid creation and the computation time. One of the major simplifications is the approximation of the free convection effects in the trapped fluid volumes in the Xmas tree assuming a solid medium in the trapped volumes and estimating a representative thermal conductivity based on the trapped fluid thermal properties, the size and the shape of the trapping cavity and other influencing flow and thermal parameters. Essentially, the approximation uses a modified thermal conductivity. The impact of this assumption and simplification on the accuracy of the heat transfer calculations can vary from case to case based on the process conditions including the temperature gradients and volume of the cavity.

The purpose of this study is the numerical validation of the modified thermal conductivity methodology described above by comparison to the results of numerical simulations which fully resolves the trapped fluid volumes by accounting for realistic flow conditions in the trapped fluid volumes including the thermal free convection.

A further objective will be to establish validity criteria for modified thermal conductivity method and where possible develop thermal conductivity correlations for volume geometries typically encountered.

The following tasks are to be considered:

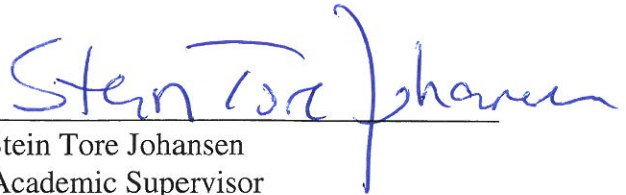
1. Get familiarized with the CFD tool ANSYS CFX (meshing, simulation, solutions and results, analysis and evaluation)
2. Literature Study
3. Analytical solution using literature correlations
4. Numerical experiments, using a simplified model where the fluid can be approximated as a rigid body with known properties with regard to thermal conductivity
5. Numerical experiments with free convection flow and heat transfer
6. Comparison and discussion of the results
7. Validation of the results of the simulations in sections 4 and section 5, compared with the results in section 3
8. Collect results and data in a well formed and detailed report

The thesis should be submitted to NTNU before 4. July 2014.

Department of Energy and Process Engineering, 14. January 2014



Olav Bolland
Department Head



Stein Tore Johansen
Academic Supervisor

Research Advisor:
Emad Gharaibah
GE Oil & Gas

Sammendrag

Hulrom på innsiden av juletrær brukt i olje- og gassnæringen inneholder som regel væske, og er dermed utsatt for varmetap i form av naturlige konveksjonsprosesser som oppstår på grunn av temperaturforskjeller mellom produksjonsfluidet og vannet på havbunnen. Slike varmeoverføringsprosesser blir i dag ofte forenklet ved å anta at de naturlige konveksjonsprosessene kan tilnærmes et fast legeme med en modifisert varmeledningsevne.

Termiske analyser av et sylinderformet hulrom bestående av vann ble i denne oppgaven utført ved hjelp av ANSYS CFX. Analytiske og numeriske løsninger av varmeoverføringsproblemet ble utarbeidet for en vertikal, lukket konsentrisk sylinder med dimensjonsforholdene $D_o/D_i = 3/2$ og $H = 10D_o$. Den indre vertikale sylinderveggen holdt en konstant, høy temperatur, og forsøk ble utført med seks forskjellige temperaturer varierende fra 50-100°C. Den ytre vertikale sylinderveggen holdt en konstant temperatur lik 4°C. Øvre og nedre sylindervegg var isolert gjennom alle forsøkene. Fluidet var lokalisert i ringrommet mellom den indre og ytre sylinderveggen.

Den analytiske løsningen baserte seg på fire litterære korrelasjoner, som hver estimerte et Nusselt tall som ble brukt til å beregne varmeffuks og varmeovergangstall for hvert temperaturtilfelle. To av korrelasjonsligningene var basert på rektangulære, lukkede beholdere, mens de to andre var basert på vertikale, konsentriske sylindere.

De numeriske verdiene baserte seg på to modeller: 1) en forenklet konduksjonsmodell med modifisert varmeovergangstall og 2) en modell basert på naturlig konveksjon. Den forenklete konduksjonsmodellen tok utgangspunkt i Nusselt tallene beregnet fra korrelasjonene for å kalkulere det effektive varmeovergangstallet. Den analytiske løsningen ble så sammenlignet med de numeriske resultatene.

Både en 2D- og 3D-modell ble utviklet, testet og sammenlignet. For den forenklete modellen basert på konduksjon, estimerte begge modellene tilnærmet samme varmeffuksverdier som forventet. En forskjell på 20% ble observert mellom modellene for fri konveksjon for en indre veggtemperatur på 100°C, hvor 2D-modellen beregnet lavere varmeffuksverdier sammenlignet med 3D-modellen. Den forenklete modellen overestimerte varmeffluksen i hulrommet med 60% i forhold til resultatene oppnådd med 3D-modellen for fri konveksjon. Korrelasjonen som antok varmeffuksverdier nærmest 3D-modellen for fri konveksjonsprosessen, hadde et avvik på 11%. Korrelasjonene for rektangulære, lukkede beholdere, ble ansett som utilstrekkelig for studiens modell.

Abstract

A free convective heat transfer model was developed in ANSYS CFX for trapped fluid volumes located inside subsea christmas trees. Analytical and numerical solutions to the heat transfer problem were generated for a vertical concentric cylinder enclosure containing water in the annulus, with aspect ratios $D_o/D_i = 3/2$ and $H = 10D_o$. The inner, vertical wall of the cylinder was fixed at a high temperature whereas the outer cylinder wall was fixed at 4°C . Different cases were investigated, with the temperature of the inner cylinder wall varying from 50 to 100°C . The upper and lower walls were insulated.

The analytical solution was based on four literature correlations, each estimating a Nusselt number that was used to compute the respective heat flux and heat transfer coefficient in each case, for comparison with the numerical results. Two of the correlations were based on rectangular enclosures, while the other two were based on vertical concentric cylinders. Numerical results were obtained with two models: 1) a simplified model with an effective thermal conductivity and 2) a fully resolved model taking into account the free convection effects. The simplified model based its effective thermal conductivity on the Nusselt numbers obtained from the literature correlations.

A 2D and a 3D model were developed, tested and compared. For the simplified model based on conduction, the 2D and 3D model estimated approximately the same heat flux values as expected. The fully resolved 2D and 3D model differed with up to 20% for a inner wall temperature of 100°C . The simplified conduction model overestimated the heat flux with up to 60%, while the correlation that predicted heat flux values closest to the fully resolved CFD model, underestimated the heat flux with 11%. The correlations for rectangular boxes were concluded as inadequate in predicting the heat flux across the annulus for the free convection model developed in this study.

Acknowledgements

I would like to express a special gratitude to Bill Antel, who turned out to be my mentor, coach and supervisor. The time he put down in always being available for all of my queries is deeply appreciated, especially since he had a full-time job to take care of in addition. Bill always found time for me, never complained about his work or rushed any of my queries. I will also thank him for his patience and understanding during this journey, and always being straight to the point - I am indebted to you.

I would also like to thank my supervisors, Professor Stein Tore Johansen at NTNU and Dr. Emad Gharaibah at GE Oil & Gas. Thank you Professor Johansen, for being patient with me and explaining everything twice if you saw the need. And thank you Dr. Gharaibah, for always doing your best in answering my many queries. A special thanks goes out to the people at GE Oil & Gas Sandvika, who let me sit with them in their office for a week, using their equipment and knowledge as much as I wished for. Thank you Mustafa Barri, for buying me lunch everyday that week I sat with you in Sandvika. Thank you Netaji Kesana, for the interest you showed in my thesis, always there with your kindness to help out as well as to gain understanding.

I also wish to express my greatest appreciation to GE Energy Bergen, for letting me sit with them in Laksevåg, Bergen, using their equipment, contacts and knowledge. Thank you for welcoming me, and let me have lunch with you as any other employee.

A special thanks goes out to my supporting family, who always stand by my side, and do what they can to keep me motivated and at my best.

Contents

| | | |
|----------|---|-----------|
| 1 | Introduction | 1 |
| 1.1 | Background | 1 |
| 1.2 | Aim and Objectives | 1 |
| 2 | Theory | 3 |
| 2.1 | Natural Convection | 3 |
| 2.1.1 | Free Convection in Enclosures | 4 |
| 2.2 | Boundary layer | 5 |
| 2.3 | Governing Equations | 7 |
| 2.3.1 | Generalized Governing Equations | 7 |
| 2.3.2 | Boundary Layer Equations | 8 |
| 2.3.3 | Governing Equations Cylindrical Coordinates | 10 |
| 2.4 | Dimensionless Parameters | 10 |
| 3 | Literature review | 13 |
| 3.1 | Empirical Correlations: Enclosures | 16 |
| 3.1.1 | Rectangular Cavities | 17 |
| 3.1.2 | Concentric Cylinders | 19 |
| 4 | Analytical solution | 22 |
| 5 | Numerical experiments | 27 |
| 5.1 | Geometry: 2D and 3D | 27 |
| 5.2 | Cases | 28 |
| 5.2.1 | Simplified Model with Modified Thermal Conductivity | 30 |
| 5.2.2 | Fully Resolved Model | 30 |
| 5.3 | Grid Description | 31 |
| 5.4 | Boundary Conditions | 33 |
| 5.5 | Numerical Model | 34 |
| 5.5.1 | Heat Flux in the Near-Wall Region | 36 |
| 5.6 | Discretization Schemes | 36 |
| 5.7 | Grid Independence | 37 |
| 5.7.1 | Convergence Control | 37 |
| 5.7.2 | Grid Refinement | 40 |
| 6 | Results | 42 |
| 6.1 | Simplified Model | 42 |
| 6.2 | Fully Resolved Model | 42 |

| | |
|---|------------|
| 7 Discussion | 50 |
| 7.1 2D vs 3D | 52 |
| 7.2 Simplified Model vs Fully Resolved Model | 54 |
| 7.3 Analytical Solution vs Fully Resolved Model | 55 |
| 7.4 Analytic Solution vs Simplified Model vs Fully Resolved Model | 57 |
| 7.5 Verification and Validation | 59 |
| 8 Conclusions | 62 |
| A Simplified Model Results | I |
| B Fully Resolved Model Results | III |

List of Figures

| | | |
|----|---|----|
| 1 | Natural convection over a vertical flat plate for $Pr > 1$, illustrating the thermal and velocity boundary layer that will arise along the plate | 6 |
| 2 | Schematic diagram from Rohsenow et al. (1998), used in establishing the correlation equations (32) and (33) | 18 |
| 3 | Schematic diagram from Bejan (2013), used in establishing correlation equations (34) | 20 |
| 4 | Schematic diagram from Deutscher (2006), as well as Nusselt number for the annulus plotted versus the Rayleigh number | 21 |
| 5 | Schematic diagram of the vertical concentric cylinder used in this study | 23 |
| 6 | Illustration of the concentric cylinder being "unrolled" | 25 |
| 7 | Heat transfer coefficients (7a) and heat flux 7b from the analytical solution | 25 |
| 8 | Nusselt number versus Rayleigh number based on the analytical solution | 26 |
| 9 | Illustration of the axisymmetrical concentric cylinder, with the 2D region that was modeled in ANSYS CFX | 28 |
| 10 | The 3D model showing the inner and outer cylinder wall with the fluid located in the annulus | 29 |
| 11 | The 2D grid with the element spacing decreasing towards the vertical cylinder walls | 32 |
| 12 | The 3D grid with inflation layers close to the vertical walls | 34 |
| 13 | Convergence history for the fine 2D grid | 38 |
| 14 | Convergence history for the medium 3D grid | 39 |
| 15 | Comparison between the physical timesteps 0.01 seconds (15a) and 0.001 seconds (15b) | 40 |
| 16 | Convergence history coarse 3D mesh | 41 |
| 17 | Temperature contour for the simplified model with the inner wall being 70°C | 42 |
| 18 | Temperature (18a) and velocity (18b) distribution with the inner wall being 70°C | 43 |
| 19 | Temperature contour for the fully resolved 2D model | 44 |
| 20 | Temperature contour for the fully resolved 3D model | 44 |
| 21 | Streamlines from the 2D model, showing the circulation occurring in the cavity | 45 |
| 22 | Streamlines from the 3D model, showing the circulation occurring in the cavity | 46 |
| 23 | Temperature and velocity distribution in the center of the cavity of the 2D and 3D models | 47 |
| 24 | Behaviour of the fluid velocity in the center of the cavity with the inner cylinder wall being 70°C | 48 |

| | | |
|----|---|----|
| 25 | Velocity streamlines occurring in the 2D (25a) and 3D (25b) cavities | 49 |
| 26 | Comparison of the heat flux appearing in the simplified 2D and 3D models | 53 |
| 27 | Comparison of the 2D and 3D fully resolved models | 54 |
| 28 | Comparison of the fully resolved 2D and 3D models with the simplified 3D model | 55 |
| 29 | Comparison of the analytical heat transfer coefficient and the heat transfer coefficient obtained with the 2D and 3D fully resolved models | 56 |
| 30 | Comparison of the heat transfer coefficients found in the analytical solution versus the heat transfer coefficient found with the 3D fully resolved model in ANSYS CFX. The red line represents the case where the values are equal | 57 |
| 31 | Comparison between the heat flux values obtained from the analytical so- lution, the simplified 3D model and the fully resolved 2D and 3D models . . | 58 |

List of Tables

| | | |
|----|--|-----|
| 1 | Coefficients of equation (36). Values of the factors C_1 , C_2 and the exponents n_1 and n_2 based on N from Eq. (37) | 21 |
| 2 | Properties of the vertical concentric cylinder. | 22 |
| 3 | Properties of water used in this study | 24 |
| 4 | Cases that were considered numerically for $T_i = 50 - 100^\circ\text{C}$. The effective thermal conductivity values, k_{eff} [W/m K], were calculated in the analytical solution in Section 4, while k_{water} is the thermal conductivity of water. | 29 |
| 5 | The effective thermal conductivity and Nusselt number based on the correlation equations in the analytical solution | 30 |
| 6 | Grid properties for the coarse, medium and fine 2D grids | 31 |
| 7 | Properties of the coarse, medium and fine 3D grids | 33 |
| 8 | Boundary conditions for the concentric cylinder used in the numerical experiments | 33 |
| 9 | Grid independence study | 41 |
| 10 | Grid convergence index | 61 |
| A1 | Heat flux at the inner cylinder wall of the simplified model | I |
| A2 | Heat flux at the outer cylinder wall of the simplified model | II |
| A3 | Heat flux at the inner cylinder wall of the fully resolved model | III |
| A4 | Heat flux at the outer cylinder wall of the fully resolved model | III |

Nomenclature

| | |
|------------|--|
| A | Area |
| C_f | Local friction coefficient |
| Gr | Grashof number |
| L | Length |
| Q | Heat transfer |
| T | Temperature |
| T_∞ | Ambient temperature |
| T_s | Surface temperature |
| ΔT | Delta temperature, $T_{hot} - T_{cold}$ |
| α | Thermal diffusivity [m^2/s] |
| β | Compressibility factor |
| \dot{q} | Volumetric generation rate of thermal energy [W/m^3] |
| Nu | Nusselt number |
| Pr | Prandtl number |
| Ra | Rayleigh number |
| Re | Reynolds number |
| μ | Dynamic viscosity [$\text{kg}/\text{s m}$] |
| ν | Kinematic viscosity [m^2/s] |
| ρ | Density [kg/m^3] |
| τ | Shear stress [Pa] |
| θ | Dimensionless temperature |
| c_p | Specific heat capacity, constant pressure [$\text{J}/\text{kg K}$] |
| g | Gravity [m/s^2] |
| h | Heat transfer coefficient [$\text{W}/\text{m}^2\text{K}$] |
| k | Thermal conductivity |

| | |
|------------------|--|
| k_{eff} | Effective thermal conductivity [W/m K] |
| p | Pressure [kg/m s ²] |
| q_s | Surface heat flux W/m ² |
| r | Radius |
| u | Velocity, x-component |
| u_∞ | Free stream velocity |
| v | Velocity, y-component |

1 Introduction

Subsea christmas trees have to face different circumstances during operation. The components are exposed to changing temperatures and pressures, which influence the behaviour of the materials and fluids. The climate is one of the biggest challenges in the oil and gas industry, as it is impossible to control. Therefore, the surroundings have to be investigated carefully, so that the subsea components can be built and produced thereafter. Properties of surrounding substances play an important role when investigating components that are to be placed on the seabed, and an investigation involves performing a thermal analysis that reveals information about the temperature distribution of the relevant components under the relevant circumstances.

1.1 Background

Investigation of the cooldown behaviour of the subsea components can be complex and time consuming, especially if large models are to be simulated using computational fluid dynamics (CFD). Assumptions and simplifications are normally utilized to reduce the complexity and hence effort that is related to an exact CFD-analysis of the problem. One of the major simplifications related to a thermal investigation of subsea christmas trees, is an approximation of the free convection effects appearing in trapped fluid volumes inside the tree. This simplification assumes that the free convection effects can be treated as a solid medium with a modified thermal conductivity, and is based on the trapped fluid flow, thermal properties and parameters, the size, and the shape of the trapping cavity. This simplification will of course impact the accuracy of the results, but its factor will vary from case to case, depending on the process conditions such as temperature gradients and volume of cavity. Quantification of thermal performance of subsea equipment is essential for insulation design and process evaluation.

1.2 Aim and Objectives

The aim of the study was to validate the results of the modified thermal conductivity methodology and a numerical solution which fully resolves the trapped fluid volumes accounting for actual flow conditions, and compare these to an analytical solution of the problem. The following tasks were to be considered:

1. Literature study to establish the existence of and validity of analytical correlations and current state-of-the-art approximation techniques
2. Familiarization with a CFD tool (CFX) and heat transfer approaches involved in the thermal analysis of subsea christmas trees. Understanding of the physics and models for free convection

3. Validation of the simplified methodology versus the approach with the fully resolved flow in the trapped fluid cavity and with free convection
4. Validate the fully resolved flow approach versus the analytical solutions for the flow velocities and develop best practices for the computation mesh generation and the CFD setup
5. Establish validity criteria for the modified thermal conductivity method

2 Theory

Wherever there exists a temperature gradient, there will also exist heat transfer. It is common to distinguish between certain heat transfer phenomena. For instance, conduction, convection, advection and thermal radiation are all related to heat transfer, but describes different heat transfer features or situations. In thermal radiation for instance, energy is emitted by a matter via electromagnetic waves or photons due to changes in electron configurations. In conduction, heat is transferred due to an energy gradient, causing molecular activity in either solids, fluids or gases. Conduction is expressed by Fourier's law given by Incropera et al. (2007):

$$q_s'' = -k_f \frac{\partial T}{\partial y} \quad (1)$$

Convection is a term that combines conduction and energy transfer in fluid or gas due to bulk or macroscopic motion, namely advection (Smith, 2009). It is related through Newton's Law of Cooling given by:

$$q_s'' = h(T_s - T_\infty), \quad (2)$$

where h is the heat transfer coefficient (see Section 2.2), T_s is the surface temperature and T_∞ is the ambient temperature or the temperature of the fluid or gas.

Convection tends to be classified into forced and free convection. In this study, the heat transfer occurring in the trapped fluid volumes happens naturally without any influence by external forces, and will therefore be categorized as free convection.

2.1 Natural Convection

Heat transfer where fluid motion is caused by density variations resulting from temperature distributions, is classified as free or natural convection. This occurs when a surface at temperature T_s interacts with a fluid at temperature T_∞ . When these temperature distributions are present, there will be a density gradient present, hence there will be fluid motion. The movement is due to a combination of local changes in density and a body force that is proportional to density (Incropera et al., 2007). The local body forces, such as gravitational and centrifugal forces, make convection currents originate (Sachdeva, 2009). These currents are dependent upon the system conditions, as well as whether the temperature gradient is stable or unstable. This means that the presence of a fluid gradient in a gravitational field does not ensure the existence of free convection currents. An unstable temperature gradient occurs if the temperature differences exceeds a critical value and buoyancy forces are dominating over the viscous forces, that is the buoyancy forces overcome the retarding influence of the viscous forces (Incropera et al., 2007). The density will then decrease in the direction of the gravitational force. If the density gradient does

not decrease in the direction of the gravitational force, conditions are stable and there is no bulk fluid motion, meaning the heat transfer occurs by conduction.

As convection could be divided into two categories, free convection can be further broken down into internal and external flows. If the flow is enclosed by solid boundaries, the flow is said to be internal, while an external flow does not have any boundaries (Burmeister, 1993). If an internal flow interacts with a surface, or boundary, at a higher temperature, the fluid close to the surface will be less dense due to fluid expansion because of increasing temperatures, causing it to rise. As soon as this happens, a boundary layer will develop. Since the fluid is enclosed, the rising fluid will entrain fluid from the quiescent region, which originally was at rest ($v = 0$ m/s). In the opposite case, that is the fluid is at a higher temperature than the surface, the fluid motion will be downwards as a result of heat transfer from the fluid to the surface, making the fluid contracting, hence becoming more dense. In both cases, a free convection boundary layer will develop as soon as the fluid rises or falls.

The general analysis of natural convection is complicated, and sometimes the only way to determine the heat transfer coefficient is through experimentation. CFD has however made it possible to determine heat transfer due to free convection by performing numerical simulations.

2.1.1 Free Convection in Enclosures

Buoyancy forces are the driving force for circulation of a fluid or gas, triggered by a density gradient. In an enclosure not influenced by any external forces, the density gradients will exist only if there are temperature gradients. If these are present, the fluid or gas within the enclosure will have local velocities. If there is a hot isothermal wall and a cold isothermal wall present in the enclosure, fluid or gas will generally rise when in contact with the hot side, and fall when interacting with the cold one, creating circulations transferring heat from the hot side to the cooler side. If the buoyancy forces are not large enough to overcome the viscous forces, there will be no circulation, and heat transfer across the enclosure will essentially be by conduction (Jiji, 2009). Heat flux due to circulation may be determined from Eq. (2), Newton's law of cooling.

Simple boundary layer theory is sometimes not sufficient in treating internal convection. The reason why is because the entire fluid or gas in the enclosure will engage and impact the convection (Faghri et al., 2010). When looking at an annular enclosure formed by two concentric cylinders at different temperatures, the flow will be circulating in the enclosure and the problem will be axisymmetric. The circulation will transfer heat from the hot side to the cold side (Jiji, 2009).

It is common today to determine the heat transfer coefficient based on literature correlations (Jiji, 2009). Literature will typically contain a lot of different correlations for the Nusselt number (see Section 2.4), which in turn is used to find the heat transfer coefficient.

These parameters are linked through

$$\text{Nu} = \frac{hL}{k}, \quad (3)$$

where h is the heat transfer coefficient, L is the characteristic length and k is the thermal conductivity. Eq. (3) describes a simple 1D model. The correlation equations may differ a lot in form from case to case because the Nusselt number depends on the geometry and flow conditions and is therefore almost impossible to generalize.

2.2 Boundary layer

Generally the motion and energy equations in heat and mass transfer problems are built upon the concept of boundary layers, known as a thin region near a surface where the temperature and velocity gradients are large (Sachdeva, 2009). The region outside the boundary layer have velocity and temperature gradients nearly equal to the flow field's free stream value. The thickness of the boundary layer may be defined as the distance from the surface at which the local velocity or temperature reaches 99% of the external velocity or temperature. In general, both the velocity boundary and layer and thermal boundary layer exist simultaneously (Sachdeva, 2009).

Velocity boundary layer When a fluid interacts with a surface, it is the surface geometry together with the flow conditions that determines the behaviour of the fluid. If the surface acts as a no slip wall, the velocity of the fluid relative to the wall is reduced to zero, due to viscosity μ , and shear stresses τ_s . Fluid particles will then retard in the adjoining fluid layers, until the effect becomes negligible. The distance from the surface to where this retarding process declines is called the boundary layer thickness, which grows with increasing distance from the leading edge of the surface. The surface shear stress, τ_s , is given from Incropera et al. (2007) by:

$$\tau_s = \mu \left. \frac{\partial u}{\partial y} \right|_{y=0} \quad (4)$$

The velocity boundary layer stems from its relation to the surface shear stress, and hence surface frictional effects must be present. The local friction coefficient is a dimensionless parameter which determines the surface frictional drag and is given as

$$C_f \equiv \frac{\tau_s}{\rho u_\infty^2 / 2} \quad (5)$$

Thermal boundary layer When a fluid interacts with a surface at a different temperature, temperature distributions will occur and a thermal boundary layer will develop. Fluid particles in contact with the surface will achieve thermal equilibrium, and exchange energy with the particles in the adjoining fluid layers. A temperature gradient is in this way developed in the fluid, creating the thermal boundary layer region. The boundary layer grows with increasing distance from the leading edge, as the heat transfer penetrates further into the free stream (Incropera et al., 2007). The thermal boundary layer and the heat transfer coefficient are related through the local surface heat flux. If the surface is a no slip wall, there is no fluid motion relative to the surface and the energy transfer occurs by conduction (Incropera et al., 2007).

Both thermal and velocity boundary layers are presented in the illustration in Fig. 1.

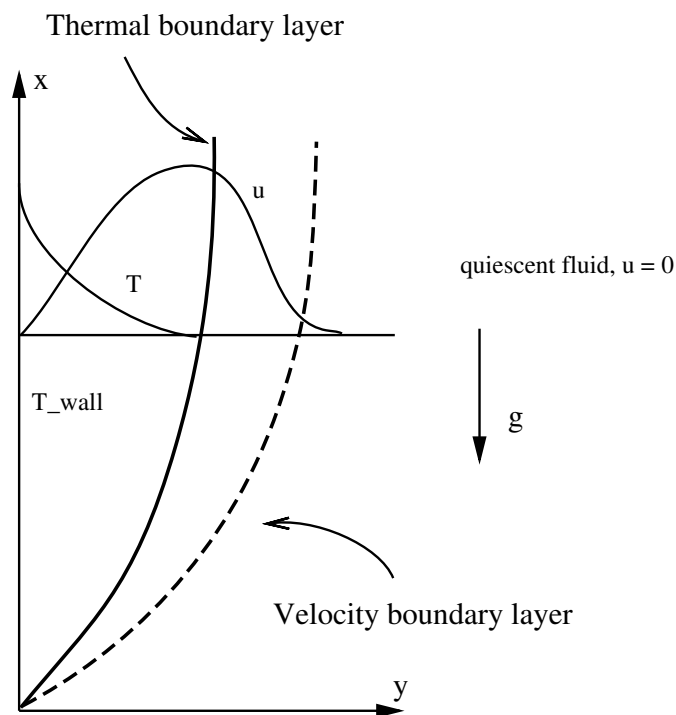


FIGURE 1: Natural convection over a vertical flat plate for $Pr > 1$, illustrating the thermal and velocity boundary layer that will arise along the plate

Although velocities tend to be rather small in free convection problems, the boundary layers are not necessarily restricted to laminar flow. Hydrodynamic instabilities may arise, leading to transition from laminar to turbulent flow (Incropera et al., 2007). The difference between them is that the laminar flow is highly ordered, while the turbulent boundary layer is more chaotic and irregular (Incropera et al., 2007). Convection transfer rates and surface friction depend strongly on the flow conditions, so having knowledge about the flow characteristics is essential. In many cases, both turbulent and laminar flow conditions

will occur in the boundary layer development, with the latter preceding the turbulent section. In this case there will be a transition zone dividing the two boundary layers, across which the conversion will occur. The conversion is due to triggering mechanisms, such as unsteady flow structures and/or disturbances originating from fluctuations in the free stream or it may be induced by surface roughness or surface vibrations (Incropera et al., 2007).

2.3 Governing Equations

2.3.1 Generalized Governing Equations

When considering flow of a viscous fluid, the law about matter not being created nor destroyed applies. For steady flow, this law requires that the flow entering a control volume is equal to the flow leaving the control volume. Because of conservation of mass, the net rate at which mass enters the control volume must equal zero at every point in the fluid (Incropera et al., 2007). This is known as the *continuity equation* and can for a 2D problem be written as:

$$\frac{\partial u}{\partial x} + \frac{\partial v}{\partial y} = 0 \quad (6)$$

where u and v are the velocities in the x - and y -directions, respectively. A second fundamental law concerning the flow of a viscous fluid is *Newton's Second Law of Motion*. This law states that the sum of all forces acting on the control volume must equal the net rate at which momentum leaves the control volume (outflow - inflow) (Incropera et al., 2007). Applying Newton's second law of motion in the x - and y -directions to a differential control volume in the fluid (Incropera et al., 2007), yields

$$\rho(u \frac{\partial u}{\partial x} + v \frac{\partial u}{\partial y}) = -\frac{\partial p}{\partial x} + \mu(\frac{\partial^2 u}{\partial x^2} + \frac{\partial^2 u}{\partial y^2}) + X \quad (7)$$

$$\rho(u \frac{\partial v}{\partial x} + v \frac{\partial v}{\partial y}) = -\frac{\partial p}{\partial y} + \mu(\frac{\partial^2 v}{\partial x^2} + \frac{\partial^2 v}{\partial y^2}) + Y \quad (8)$$

Just as with mass, energy can neither be created nor destroyed, but only change form from one to another. As a third law and part of the governing equations family is the *thermal energy equation*. When this equation is applied to a differential control volume in a moving fluid under steady conditions, it expresses that the net rate at which energy enters the control volume, plus the rate at which heat is added, minus the rate at which work is done by the fluid in the control volume (Incropera et al., 2007), is equal to zero. For an incompressible fluid with constant properties, this yields:

$$\rho c_p \left(u \frac{\partial T}{\partial x} + v \frac{\partial T}{\partial y} \right) = k \left(\frac{\partial^2 T}{\partial x^2} + \frac{\partial^2 T}{\partial y^2} \right) + \mu \Phi + \dot{q} \quad (9)$$

where \dot{q} is the thermal energy generation which will be zero. $\mu\Phi$ is the viscous dissipation defined as

$$\mu\Phi \equiv \mu \left\{ \left(\frac{\partial u}{\partial y} + \frac{\partial v}{\partial x} \right)^2 + 2 \left[\left(\frac{\partial u}{\partial x} \right)^2 + \left(\frac{\partial v}{\partial y} \right)^2 \right] \right\} \quad (10)$$

The governing equations constitutes the Navier Stokes equations which are common to use in CFD-analyses. When these are solved three-dimensionally, an extra equation is needed for the z -momentum as well as extra terms added to the continuity equation and the energy equation accounting for fluid movement in this direction also. The Navier Stokes equations describe fluid motion, and can be used for solving unsteady and compressible flow problems as well as steady and incompressible flow problems.

2.3.2 Boundary Layer Equations

To be able to solve Eqs. (6), (7), (8) and (9), information relative to the problem is essential. For free convection problems, the following may be approximated according to Jiji (2009):

1. Density is assumed constant except in evaluating gravity forces
2. An approximation relating density changes to temperature changes is used in formulating buoyancy force in the momentum equation
3. Dissipation effect is neglected in the energy equation

If looking at a vertical plate with length $L = x$, where the gravity force acts in the negative x -direction, and a laminar, steady, two-dimensional and incompressible flow, but with the exception as assumption number 1 in the above list, Eq. (7), with body force $X = -\rho g$, can be written as

$$u \frac{\partial u}{\partial x} + v \frac{\partial v}{\partial y} = -\frac{1}{\rho} \frac{dp_\infty}{dx} - g + \nu \frac{\partial^2 u}{\partial y^2}, \quad (11)$$

where dp_∞/dx is the free stream pressure gradient, that is the pressure in the the quiescent region outside the boundary layer where $u = 0$ m/s (Incropera et al., 2007). The pressure gradient then reduces to

$$\frac{dp_\infty}{dx} = -g\rho_\infty \quad (12)$$

Eq. (12) indicates that the change in pressure over a distance dx is equal to the weight per unit area of the fluid element (Sachdeva, 2009). Substituting Eq. (12) into (11), the expression becomes

$$u \frac{\partial u}{\partial x} + v \frac{\partial v}{\partial y} = g \left(\frac{\rho_\infty}{\rho} - 1 \right) + \nu \frac{\partial^2 u}{\partial y^2} = g \left(\frac{\rho_\infty - \rho}{\rho} \right) + \nu \frac{\partial^2 u}{\partial y^2} \quad (13)$$

Flow originates because of the variable density ρ , and if these variations are due only to temperature variations, the buoyancy force (first term on right-hand side) may be related to a fluid property known as the *volumetric coefficient of thermal expansion*, or the *compressibility factor* β (Incropera et al., 2007):

$$\beta = -\frac{1}{\rho} \left(\frac{\partial \rho}{\partial T} \right)_p \quad (14)$$

The change in density, $\Delta\rho = \rho_\infty - \rho$, can be expressed in terms of this coefficient as:

$$\Delta\rho = -\rho\beta\Delta T \quad (15)$$

$$\Rightarrow \left(\frac{\rho_\infty - \rho}{\rho} \right) = -\beta(T_\infty - T) \quad (16)$$

Eq. (15) can be simplified to what is known as the *Boussinesq approximation*, that is assumption 2, relating density changes to temperature changes:

$$\rho_\infty - \rho \approx \rho\beta(T - T_\infty) \quad (17)$$

Substituting Eq. (15) into (13) the *x-momentum equation* becomes

$$u \frac{\partial u}{\partial x} + v \frac{\partial v}{\partial y} = g\beta(T - T_\infty) + \nu \frac{\partial^2 u}{\partial y^2} \quad (18)$$

Assumption 3 in the list is exploited in the energy equation. The viscous dissipation expresses the net rate of work done by the element on the surroundings (Jiji, 2009), and may be neglected due to the small velocities that are associated with free convection (Incropera et al., 2007). It is assumed that the x-direction velocity and temperature changes from their surface values to their free stream values very fast, or over small distances, which in turn will result in an assumption about small boundary layer thicknesses relative to the size of the object it develops upon. The gradients normal to the object's surface are much larger than those along the surface, meaning these can be neglected. Hence, the *energy equation* becomes

$$u \frac{\partial T}{\partial x} + v \frac{\partial T}{\partial y} = \alpha \frac{\partial^2 T}{\partial y^2}, \quad (19)$$

where $\alpha = k/\rho c_p$. Thus, the governing equations for two-dimensional laminar boundary layer free convection are the continuity equation (6), x-momentum (18) and the energy

equation (19), summarized as:

$$\begin{aligned}
\text{Continuity :} & \quad \frac{\partial u}{\partial x} + \frac{\partial v}{\partial y} = 0 \\
x - \text{momentum :} & \quad u \frac{\partial u}{\partial x} + v \frac{\partial v}{\partial y} = g\beta(T - T_\infty) + \nu \frac{\partial^2 u}{\partial y^2} \\
\text{Energy :} & \quad u \frac{\partial T}{\partial x} + v \frac{\partial T}{\partial y} = \alpha \frac{\partial^2 T}{\partial y^2}
\end{aligned}$$

2.3.3 Governing Equations Cylindrical Coordinates

The aspect ratio of a cylinder will impact the thermal boundary layer thickness. If the diameter is much larger than the height, the thermal boundary layer thickness will be much smaller than the radius of the cylinder (Faghri et al., 2010). When this is the case, correlations for natural convection over a vertical flat plate can be used to calculate the natural convection over a vertical cylinder according to Faghri et al. (2010), because the flow over the cylinder will behave similar to the flow over a plate. The limits for when this is applicable are referred to as *thick cylinder limit* and *thin cylinder limit*. For fluids with $Pr > 1$, the condition under which the correlation for heat transfer over a flat plate is applicable is $D/H > Ra_H^{-1/4}$. If $D/H < Ra_H^{-1/4}$ however, the boundary layer thickness will be comparable to the radius of the cylinder and the effect of the surface curvature must be taken into account (Faghri et al., 2010). A cylindrical coordinate system is then needed, as given below:

$$\text{Continuity :} \quad \frac{\partial u}{\partial x} + \frac{1}{r} \frac{\partial(vr)}{\partial y} = 0 \quad (20)$$

$$\text{Momentum :} \quad u \frac{\partial u}{\partial x} + \frac{v}{r} \frac{\partial(ur)}{\partial r} = g\beta(T - T_\infty) + \nu \frac{1}{r} \frac{\partial}{\partial r} \left(r \frac{\partial u}{\partial r} \right) \quad (21)$$

$$\text{Energy :} \quad u \frac{\partial T}{\partial x} + \frac{v}{r} \frac{\partial(Tr)}{\partial y} = \alpha \frac{1}{r} \frac{\partial}{\partial r} \left(r \frac{\partial T}{\partial r} \right) \quad (22)$$

The aspect ratio of the height of the cavity to the spacing between the hot and cold side, H/δ , is closely related to the heat transfer and will be one of the key parameters governing the Nusselt number (Jiji, 2009).

2.4 Dimensionless Parameters

Knowing values of different dimensionless parameters can be very useful when investigating heat transfer problems, as they can predict the fluid's behaviour. A parameter essential in boundary layer theory, is the one representing the ratio of the inertia to viscous forces,

namely *Reynolds number*, given by (Incropera et al., 2007):

$$\text{Re}_L = \frac{\rho u_\infty L}{\mu} \quad (23)$$

For large values of Re_L , the inertia forces are expected to dominate, while for small values of Re_L , the viscous forces are the dominating ones. This means that for small Re_L , the viscous forces are large relative to the inertia forces, so that small disturbances are prevented to amplify in the streamwise direction, maintaining the laminar flow. With increasing Re_L , however, the inertia forces dominate, making the viscous forces less significant in comparison. The effect of this can be that small disturbances in the flow is amplified, so that transition is likely to occur (Incropera et al., 2007). The magnitude of Reynolds number will also affect the velocity boundary layer thickness δ . Increasing Re_L indicates inertia forces influencing more than viscous forces, causing the effects of viscosity not penetrating as far into the free stream, which in turn diminishes the value of δ . For flow in a circular tube, laminar flow is in general defined as $\text{Re}_D \lesssim 2300$ (Incropera et al., 2007).

Reynolds number is an important parameter in forced convection, where the relative motion between the fluid and the surface is maintained by external means. When it comes to natural convection, however, there is another important parameter one will have to pay attention to, called Grashof number. Grashof number is sort of natural convection's Reynolds number, and is defined as Re^2 . As mentioned in section 2.1, the only driving force in free convection is the buoyancy force. The Grashof number provides a measure of the ratio of buoyancy forces to viscous forces in the velocity boundary layer (Sachdeva, 2009) and is given by

$$\text{Gr}_L \equiv \frac{g\beta L^3(T_s - T_\infty)}{\nu^2}, \quad (24)$$

If both forced and free convection effects are present at the same time, the situation becomes more complex. The combination of these will have to be considered when

$$\frac{\text{Gr}_L}{\text{Re}_L^2} \approx 1 \quad (25)$$

If Eq. (25) is much less than 1 ($\ll 1$), forced convection is of greater influence than the free convection effects, which then may be neglected. Conversely, if Eq. (25) is much greater than 1 ($\gg 1$), one will only have to consider the free convection effects and can neglect the forced ones.

Another important parameter in convection problems is the Nusselt number, given as the product of the heat transfer coefficient h and characteristic length L , divided by the

thermal conductivity of the fluid k_f :

$$\text{Nu} \equiv \frac{hL}{k_f}, \quad (26)$$

and provides a measure of the convection heat transfer occurring at the surface, that is the ratio of convection to pure conduction heat transfer (Incropera et al., 2007). It is equal to the dimensionless temperature gradient and is therefore of great significance when investigating the thermal boundary layer. As Eq. (26) implies, knowledge of Nu can help find the local convection coefficient h , which in turn can help find the local heat flux. An empirical correlation for the Nusselt number for the relevant geometry is therefore effective in convection problems.

If the free convection effects are of greater influence than the forced convection effects, that is $\text{Gr}_L/\text{Re}_L^2 \gg 1$, the Nusselt number is a function of the Grashof number Gr and the Prandtl number Pr, written as

$$\text{Nu} = f(\text{Pr}, \text{Gr}) \quad (27)$$

The Prandtl number is the ratio of the kinematic viscosity to the thermal diffusivity, and is given by

$$\text{Pr} = \frac{\nu}{\alpha} = \frac{c_p \mu}{k} \quad (28)$$

As opposed to the Nusselt number, the Prandtl number is only dependent on the fluid and its state. One can see from Eq. (28) that $\text{Pr} \ll 1$ indicates that the thermal diffusivity dominates, while $\text{Pr} \gg 1$ indicates that the momentum diffusivity dominates.

Sometimes a parameter called Rayleigh number Ra is used instead of Grashof number in free convection heat transfer. A critical value of the Grashof number is used to indicate transition from laminar to turbulent flow in free convection (Sachdeva, 2009), and this transition is common to correlate in terms of the Rayleigh number, which is the product of the Grashof and Prandtl number:

$$\text{Ra}_L = \text{Gr}_L \cdot \text{Pr} = \frac{g\beta(T_s - T_\infty)L^3}{\nu\alpha} \quad (29)$$

For vertical plates, the transition from laminar to turbulent flow may be given by a critical $\text{Ra}_{x,c}$

The critical Rayleigh number Ra_c will depend on the geometry and aspect ratios. For a rectangular parallelepiped cavity, Rohsenow et al. (1998) suggest that when H/L and $W/L \rightarrow \infty$, $\text{Ra}_c \rightarrow 1708$, and if H/L and $W/L \rightarrow 0$, $\text{Ra}_c \rightarrow 10^6$. Approximately the same values are suggested for horizontal circular cavities also. This indicates that a small aspect ratio yields a large critical Rayleigh number.

3 Literature review

A Computational Fluid Dynamics (CFD) approach predicts the thermal performance of subsea equipment by numerically determining the local convective coefficients between equipment and sea water.

Flow assurance is critical for subsea production due to the temperature and pressure differences between the seawater and the production fluid. Deepwater subsea installations may be placed up to 3000 meters below topside, which corresponds to high operation pressures ranging from 60 - 207 MPa (Lu et al., 2011). With operating temperatures ranging from 149-177°C, this can be classified as a High Pressure and High Temperature (HPHT) environment (Lu et al., 2011). The cold seawater surrounding the subsea installations cause large heat losses, and thermal insulation is required to minimize the losses during production. The high pressure conditions are critical for hydrate formation, and the insulation is also needed to prevent this from happening when temperatures decrease. However, subsea components are of a complex nature, making it difficult to insulate it fully everywhere. This may cause cold spots to be created, which are spots experiencing greater heat losses due to little or no insulation. The cold spots are a source to hydrate formation and flow blockages, and hence unpreferable. Thermal insulation and accurate prediction of temperature evolution during production and cool-down operations are therefore required, which calls for a reliable thermal analysis to ensure correct design and designated thermal performance, together with structural reliability and production assurance. Seals and electronic sensors are especially exposed to critical temperatures (Lu et al., 2011).

The Finite Element Analysis (FEA) approach is normally used in the thermal analysis for subsea equipment (Lu et al., 2011), where the well stream is regarded as a solid body. This simplifies the analysis, by using an approximated value for the heat convection between subsea components and surrounding seawater. This way, the convection contribution or trapped fluids are either ignored or estimated by empirical correlations. Another common simplification frequently done in these analyses is treating thermal properties as temperature-independent constants (Lu et al., 2011). Simplifications like these are all contributors to introducing uncertainty to the result. With this approach, only the conduction equation is solved in the solid domain (Lu et al., 2011). An equivalent thermal conductivity for the production fluid is introduced as an approximation to the real life situation. Interactions between subsea equipment and surrounding environs use an approximation for the heat convection coefficient through an empirical correlation (Lu et al., 2011). Fluids trapped inside the subsea equipment are frequently assumed stationary and treated as if behaving like solid bodies of equivalent heat conductivity. The problem is that the heat transfer rate vary with the geometry and orientation of the enclosures, and it is close to impossible to standardize its precise solution.

In contrast to FEA, the CFD approach solves both the conduction equation in the

solid domain and the flow equations in the fluid domain, and in this way accounts for both conduction and convection contribution of the trapped fluids (Lu et al., 2011). The CFD methodology is more detailed relative to thermal properties and a more realistic thermal behaviour can be obtained by simulating the problem with a CFD-tool. This involves a numerical solution of the thermal energy problem, where the converged solution has to be validated against experimental data or theoretical solutions because an approximation to the exact solution has been made in each step during the simulation process.

In practical applications, well stream flowing inside the production bore involves forced heat convection, and experiences significant heat losses due to current and buoyant flows of the seawater and internal heat exchange due to circulation of various trapped fluids will also be present (Lu et al., 2011). Some of the challenges with solutions to thermal analysis of complex subsea equipment are related to the high computational demand, although the computational power in the last decades has been advanced due to larger domains and more complex underlying physics (Lu et al., 2011).

Thermal properties of the associated materials may be temperature-dependent and vary significantly as a temperature gradient exists from the production bore to the seawater, which normally holds a temperature of approximately 4°C. Complexities arises because the non-linearity of thermal-fluid interactions increases, and it becomes challenging to precisely quantify the thermal performance. Steel structures such as subsea trees, chokes, valves, manifolds and wellheads will quickly lose stored internal heat as well as the latent fluid thermal energy to the colder environs. Hydrates might form over a certain time period when temperatures are low (15.5 - 26.6°C range), which could cause blockage of passageway and leading to impediment of production. Subsea christmas trees are complex in structure and may be subdivided into sub-assemblies which contain temperature-sensitive components with specific qualification temperatures and characteristic thermal behaviour, making them especially vulnerable to temperature changes.

Pantokratoras (2000) investigated laminar natural convection of both pure and saline water along a vertical isothermal cylinder in the temperature range 0°C and 20°C, taking into account the temperature dependence of fluid density, kinematic viscosity and thermal diffusivity. The investigation was carried out with a finite difference solution of the boundary layer equations using cylindrical coordinates (that is Eq. (20), (21) and (22)) and the Boussinesq approximation discussed in Section 2.3.2.

According to Pantokratoras (2000), the density-temperature relationship for pure water is linear for high temperatures, while non-linear at low temperatures. With decreasing temperatures, the density of water increases until it reaches a maximum at 3.98°C. From thereon, the density starts decreasing again when temperatures decrease further down to 0°C. If a system is experiencing temperatures between 0°C and 3.98°C, one will not obtain accurate solutions if the density-temperature relationship is considered constant.

Pantokratoras (2000) found that the wall heat transfer increased as the Pr number

increased, but as the ambient temperature approached maximum density temperature of water, the heat transfer also decreased and was at a minimum when 3.98°C was reached. So at maximum water density temperature, the heat transfer was at a minimum. The wall heat transfer was then seen to increase from this point on, as the ambient temperature was further decreased and Pr increased. In his study, he also found that the wall shear stress decreased with decreasing ambient water temperatures until it reached a minimum around the temperature of maximum density. From that point on, the wall shear stress increased, approaching the linear density-temperature curve.

Pantokratoras (2000) concluded that the variation of ν , α and ρ had a strong influence on the free convection characteristics and the wall heat transfer and shear stress values. This influence increased with increasing temperature differences between the cylinder and the ambient water. If the curvature parameter was increased, the wall heat transfer would also increase for a given Pr number. The velocity profiles were seen to become narrower for temperatures exceeding maximum density temperature for increasing Pr numbers, while wider for temperatures below this value. The variation of viscosity and thermal diffusivity also showed to be significant for the wall heat transfer and the shear stresses. When the temperature differences between the cylinder and the ambient water increased, the influence of the variations would also increase, and vice versa. As the ambient temperature decreased, the differences between saline water ($s = 40\%$) and pure water (with saline water having a higher value of Pr than pure water) were seen to increase. At temperatures in the linear density-temperature region (high temperatures) and $\text{Pr} = 7$ (pure water) and $\text{Pr} = 7.28$ (saline water), the difference in heat flux was approximately 1%. For lower temperatures and $\text{Pr} = 10.99$ (pure water) and $\text{Pr} = 11.21$ (saline water), the difference reached approximately 20%.

Hadjadj et al. (1999) presented in their study a numerical investigation of laminar natural convection in two concentric vertical cylinders, using a control volume finite difference method and a Semi-Implicit Method for Pressure Linked Equations (SIMPLE) algorithm to solve the Navier-Stokes equations, linking the two-dimensional continuity and momentum equations. The effect of changing parameters such as Prandtl number, Rayleigh number and aspect ratios were studied through the variation of temperature and flow patterns within the annular cavity. A fully developed laminar free convection flow in an open ended vertical concentric cylinder was studied for $0.01 \leq \text{Pr} \leq 10$, $1 \leq \text{Ra} \leq 10^5$ and $5 \leq A \leq 10$, with air as fluid. It was concluded that changes in the aspect ratio $A = H/r_o$, where H was the height of the cylinder, and r_o the radius of the outer cylinder, did not have a major influence on the flow structures and isotherm patterns, but maximum stream function values increased with A . The motion only consisted of a single vortex in each case tested. Hadjadj et al. (1999) obtained general correlation equations for the local and average Nusselt number, respectively, based on the ranges of Pr, Ra and

A tested:

$$\text{Nu} = 0.524 \text{ Ra}^{0.248} \quad (30)$$

$$\overline{\text{Nu}} = 0.133 \overline{\text{Ra}}^{0.33} A^{-0.32} \quad (31)$$

These relations show that the average and local Nusselt numbers increases with decreasing aspect ratios and increasing Rayleigh numbers.

3.1 Empirical Correlations: Enclosures

Today there exists a lot of different empirical correlations regarding natural convection. Many of these are results of experimental measurements, which in general will give the most correct answer ompared to alternative approaches, at least for that specific case and if executed correctly. A numerical solution, for example one obtained from CFD, may also yield good results, depending on the model, grid, setup and solver. Mathematical analyses of natural convection problems tend to be very complex, and even the simplest case of laminar free convection over an isothermal vertical plate require numerical integration (Jiji, 2009).

Experiments are therefore important in solving these types of problems, resulting in empirical correlations to be used in later computations and solutions procedures. The fluid behaviour depends strongly on the geometry, and the correlations may yield incorrect predictions of the thermal performance if unsuitable for the problem where utilized. Although a lot of correlations exist and have been carefully tested, free convection problems are difficult to generalize. As far as correlations are concerned, it is important to keep in mind that equations established based on experimentally determined data may predict inaccurate values of the heat transfer coefficient h , due to uncertainties and errors different systems experiencies compared to the system the correlation originates from (Jiji, 2009).

An increase in the wall temperature of a cavity is characterized by a temperature wave, distributing in the fluid and causing temperature differences within the fluid. The wave will eventually reach the center of the cavity, and after some time the differences in temperature between the hot wall and the center will tend to a constant value, called the process' quasi-steady regime of flow and heat transfer (Martynenko and Khramtsov, 2005). The core is normally characterized by a horizontally uniform temperature. The main change in temperature occurs in a boundary layer near the wall, and will often overlap the core, complicating the free convection problem in closed cavities.

In the top and bottom regions of cavities formed as spheres, there will be stagnant zones present. At the lower boundary, cold liquid will be collected, while in the upper part of the enclosure there will be a heated stagnant zone. The presence of these zones reduces the heat transfer and can lead to overheating (Martynenko and Khramtsov, 2005).

Free-convective heat transfer in cavities is accompanied by thermal stratification in the

core of the enclosed flow, with the temperature of the upper liquid layers exceeding the average values (Martynenko and Khramtsov, 2005). The convective flow brings the hot liquid to the upper layer and noticeably distorts the temperature field which becomes two-dimensional or three-dimensional due to this effect (Martynenko and Khramtsov, 2005) (helt likt). When a quasi-stationary regime is attained in the upper part of the cavity into which the hot liquid enters, the wall temperature can be higher compared with the heat transfer only due to the thermal conductivity.

As the cylinder height increases, the stratification depends less on H/D (Martynenko and Khramtsov, 2005). In the case of a long process of heat supply, it becomes necessary to take into account a change in pressure during the heating process, which will tend to influence the heat transfer (Martynenko and Khramtsov, 2005).

3.1.1 Rectangular Cavities

Rohsenow et al. (1998) suggested that for heat transfer in vertical rectangular parallelepiped cavities, that is $\theta = 90^\circ$ based on the schematic diagram from Rohsenow et al. (1998) presented in Figure 2, and with properties $H/L \geq 5$ and $W/L \geq 5$, fluids undergoing a natural convection can be expressed by a Nusselt number given by

$$\text{Nu} = \left[1, 0.36 \text{Pr}^{0.051} \left(\frac{L}{H}\right)^{0.36} \text{Ra}^{0.25}, 0.084 \text{Pr}^{0.051} \left(\frac{L}{H}\right)^{0.1} \text{Ra}^{0.3} \right]_{max}, \quad (32)$$

for fluids with $\text{Pr} \geq 4$, and $\text{Ra} (H/L)^3 < 4 \times 10^{12}$. The above equation (32) is based on experimental data, and is tested for values of H/L ranging from 5 – 47.5. The middle term is tested for $3 < \text{Pr} < 40,000$, while the last term is tested for $3 \lesssim \text{Pr} \lesssim 200$. If $\text{Ra} (H/L)^3 > 4 \times 10^{12}$, the following relation is suggested to be used instead:

$$\text{Nu} = 0.039 \text{Ra}^{1/3} \quad (33)$$

Eq. (33) is however only tested for $\text{Pr} = 5$, and may according to Rohsenow et al. (1998) underpredict measurements by as much as 20 percent. For $5 \leq H/L < 10$, Eq. (32) and (33) are most accurate for adiabatic walls.

If $H/L \leq 40$, the flow tend to enter a laminar boundary layer regime before becoming unstable and entering the turbulent transition regime (Rohsenow et al., 1998). Laminar boundary layers will then occur on each plate with an essentially stationary core between them, which is nearly isothermal in the horizontal direction while having a positive gradient in the vertical direction. The flow will encounter the conduction regime followed by laminar boundary layer and last turbulent boundary layer as Ra increases (Rohsenow et al., 1998). If $H/L \geq 40$, the conduction regime becomes unstable at a critical Rayleigh number Ra_c . A further increase in Ra past Ra_c will lead to a turbulent transition regime and finally into a fully developed turbulent boundary layer regime, which is characterized by

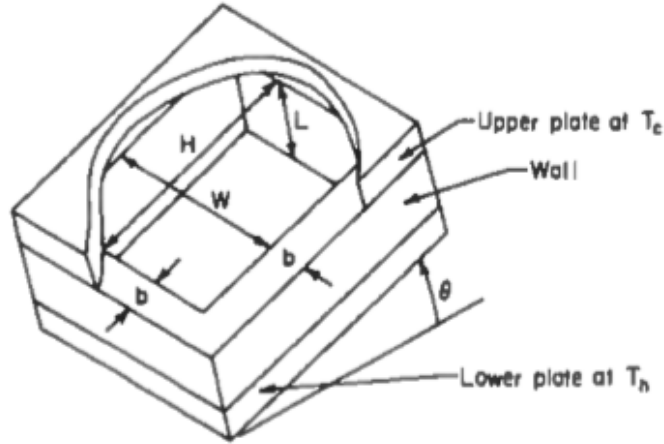


FIGURE 2: Schematic diagram from Rohsenow et al. (1998), used in establishing the correlation equations (32) and (33)

turbulent boundary layers on each plate and a well-mixed core between them (Rohsenow et al., 1998).

In rectangular enclosures heated from the side, there are various heat transfer regimes that may occur depending on the system. The Rayleigh number, Ra , plays an important role when deciding which one is applicable. For $Ra_H^{-1/4} < H/L < Ra_H^{1/4}$, where H is the height of the enclosure and L the transversal extent of the enclosure (see Figure 3), the flow pattern will be characterized by boundary layers on all four walls, while the core of the fluid remains stagnant and stratified (Faghri et al., 2010). Ra_H is the Rayleigh number based on the height of the enclosure. The heat transfer will occur through boundary layer convection, and is affected by the flow pattern. For $H/L > Ra_H^{1/4}$ (tall systems), there will be distinct boundary layers on top and bottom walls, while for $H/L < Ra_H^{-1/4}$ (shallow systems) there will be two horizontal wall jets flow in opposite directions (Faghri et al., 2010). For high Rayleigh numbers, Bejan (2013) found a correlation based on an insulated cavity at top and bottom, with a vertical side exposed to periodic heating and the opposite one at a lower temperature valid for fluids with high Ra_H numbers and with $Pr > 1$. Bejan (2013) did a further analysis of already existing relations in boundary layer theory. He studied equations established by A. E. Gill in 1966, who managed to evade the nonlinearity of the energy equation by utilizing a technique called Oseen-linearization (Bejan, 2013). Gill invoked the energy integral

$$\int_0^\infty \left(u_* \frac{\partial T_*}{\partial x_*} + v_* \frac{\partial T_*}{\partial y_*} \right) dx_* = - \left(\frac{\partial T_*}{\partial x_*} \right)_{x_*=0},$$

where the subscript ”* ” indicates non-dimensional quantities. Together with the above integral, two symmetry conditions were used. The symmetry conditions said that the

boundary layer solution on the cold side, that is the temperature and velocity, had to approach the free stream velocity and temperature values when $x_* \rightarrow \infty$. Bejan (2013) found that Gill's equations gave valid velocity solutions in the boundary layer only, and that the results were improper to use in the corners. Bejan (2013) investigated the heat transfer result of Gill's analysis, and found that the overall heat transfer rate across the enclosure, which never was stated by Gill, could be written as

$$\begin{aligned} q' &= k \int_{-H/2}^{H/2} \left(-\frac{\partial T}{\partial x} \right)_{x=0} dy \\ &= 0.364k \Delta T \text{Ra}_H^{1/4} \end{aligned}$$

He further said that a relationship for the overall $\overline{\text{Nu}}$ correlations was, from the majority of experimental and numerical studies, reported to be

$$\overline{\text{Nu}} = \frac{q'}{q_{\text{pure conduction}}} = \frac{q'}{(kH\Delta T)/L},$$

which led to a correlation for the average Nusselt number:

$$\overline{\text{Nu}}_H = 0.364 \left(\frac{L}{H} \right) \text{Ra}_H^{1/4}, \quad (34)$$

valid for a system characterized by $\text{Ra}_H^{-1/4} < H/L < \text{Ra}_H^{1/4}$.

3.1.2 Concentric Cylinders

Hadjadj et al. (1999) suggested the following correlation for the average Nusselt number $\overline{\text{Nu}}$ for an annular cavity formed by a vertical concentric cylinder:

$$\overline{\text{Nu}} = 0.133 \overline{\text{Ra}}_L A^{-0.32}, \quad (35)$$

where $A = H/r_o$ is the aspect ratio, H is the height, and r_o the outer radius of the concentric cylinder. Eq. (35) was established by numerical studies for laminar fully developed natural convection in an open-ended vertical concentric cylinder. The governing equations (Navier-Stokes) were solved by adopting the iterative SIMPLE algorithm. The average Nusselt number is defined by Hadjadj et al. (1999) as

$$\overline{\text{Nu}} = \frac{\bar{h} \cdot H}{k} = - \int_0^A \frac{\partial \theta}{\partial R} dX$$

where X and R are dimensionless variables on the form $X = x/r_o$ and $R = r/r_o$, and the dimensionless temperature $\theta = (T - T_A)/(T_E - T_A)$, with T_A being ambient temperature and T_E being entrance temperature of the fluid, which enters at the bottom of the annulus.

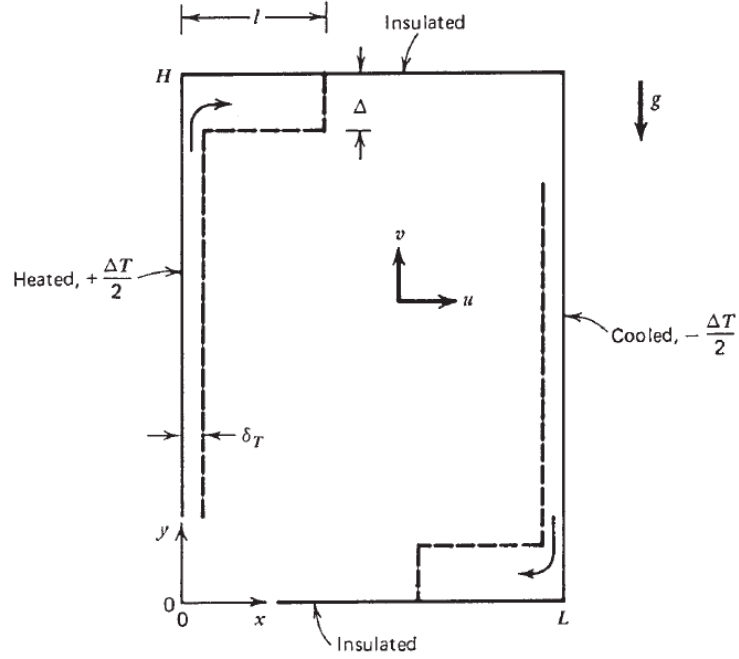


FIGURE 3: Schematic diagram from Bejan (2013), used in establishing correlation equations (34)

For the problem, Hadjadj et al. (1999) used the following boundary conditions:

$$\begin{aligned}
 U = V = 0 & && \text{on all walls} \\
 \frac{\partial U}{\partial R} = \frac{\partial V}{\partial R} = \frac{\partial P}{\partial R} = \frac{\partial \theta}{\partial R} = 0 & && \text{for } r = 0 \\
 \frac{\partial \theta}{\partial R} = 0 \text{ (In)}, \frac{\partial \theta}{\partial R} = \frac{q}{k} \text{ (Out)} & && \text{for } r = r_i \\
 k_{ai} \frac{\partial \theta}{\partial R} = k_{al} \frac{\partial \theta}{\partial R} & && \text{for } r = r_o,
 \end{aligned}$$

where k_{ai} and k_{al} were the fluid thermal conductivity and material thermal conductivity, respectively.

According to VDI-Wärmeatlas (2006), the dimensionless heat transfer coefficient Nu in enclosed vertical annular gaps can be expressed by Eq. (36), if the flow of heat is from the inside to the outside:

$$Nu_s = \frac{C_1 Gr_s Pr \left(\frac{h}{s}\right)^2}{C_2 \left(\frac{h}{r_a}\right)^4 \left(\frac{r_i}{h}\right) + \left[Gr_s Pr \left(\frac{h}{s}\right)^3\right]^{n_1} \left(\frac{r_i}{h}\right)^{n_2}}, \quad (36)$$

where the factors C_1 and C_2 , and the exponents n_1 and n_2 are dependent on the size of

the constant N given by

$$N = \left[\text{Gr}_s \text{Pr} \left(\frac{h}{s} \right)^3 \right]^{-0.25} \left(\frac{h}{r_i} \right) \quad (37)$$

As seen in Section 2.4, $\text{Ra} = \text{Gr} \cdot \text{Pr}$, so Eq. (36) (and Eq. (37)) is dependent on the Rayleigh number and aspect ratios of the cylinder. Table 1 presents the constants in Eq. (36) given by the value of N from Eq. (37).

| | C_1 | C_2 | n_1 | n_2 |
|------------------|-------|-------|-------|-------|
| $N < 0.2$ | 0.48 | 854 | 0.75 | 0 |
| $0.2 < N < 1.48$ | 0.93 | 1646 | 0.84 | 0.36 |
| $1.48 < N$ | 0.49 | 852 | 0.95 | 0.80 |

TABLE 1: Coefficients of equation (36). Values of the factors C_1 , C_2 and the exponents n_1 and n_2 based on N from Eq. (37)

The correlation in Eq. (36) was established by experiments, and is considered as a state of the art engineering method to determine heat transfer in vertical annuli. This is considered to be the correlation in closest relation to the free convection model developed and investigated in this paper. Figure 4 presents the schematic diagram that the experiment was based upon, as well as the Nusselt number versus the Ra number, both based on the annular gap spacing, for different aspect ratios. The graphs imply that for increasing Rayleigh numbers, the dimensionless heat transfer coefficient will also increase, that is the convection effects become more salient.

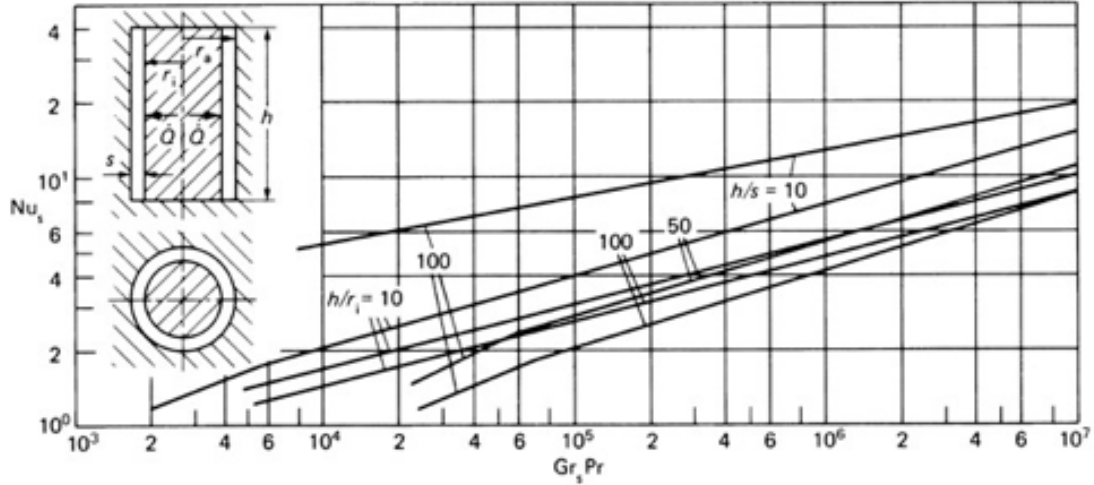


FIGURE 4: Schematic diagram from Deutscher (2006), as well as Nusselt number for the annulus plotted versus the Rayleigh number

4 Analytical solution

As seen in Section 3.1, there are different correlations published for different geometries. Some of these are generated from experiments and some from numerical simulations. This may lead to disagreement between correlations for similar geometries due to different circumstances under which these correlations were obtained. Correlations often come with certain restrictions and areas of application. Definitions of different dimensions in one model will have to correspond with the model used to obtain the correlation. An example is the Ra number, which includes a characteristic dimension. The Nu number is an expression on the form seen in Eq. (27), thus if the characteristic dimension is wrong, this would lead to errors in the following equations and final result.

A schematic diagram of a two-dimensional closed, vertical concentric cylinder is presented in Fig. 5.

An analytical solution of the free convection model may be obtained by using various correlations and set up a simplified 1D-model to predict the heat transfer behaviour. The correlations are often equations for the Nusselt number of the flow, and the heat transfer coefficient h and heat transfer Q can then be obtained by using the following equations, respectively:

$$h = \frac{\text{Nu} \cdot k}{L} \quad (38)$$

$$Q = h A (T_{hot} - T_{cold}) \quad (39)$$

Table 2 presents properties of the concentric cylinder used as model in this study. The inner wall temperature refers to the inner cylinder with diameter D_i , and varied from 50-100°C with a 10°C step from case to case, giving 6 different temperature gradients and cases.

| | Model |
|-------------------------------|-------------|
| Outer diameter, D_o | 40 mm |
| Inner diameter, D_i | $2D_o/3$ |
| Height, H | $10D_o$ |
| Annular gap, D_a | $D_o - D_i$ |
| Aspect ratio, AR | H/D_a |
| Outer wall temperature, T_o | 4°C |
| Inner wall temperature, T_i | 50-100°C |
| Fluid | Water |

TABLE 2: Properties of the vertical concentric cylinder.

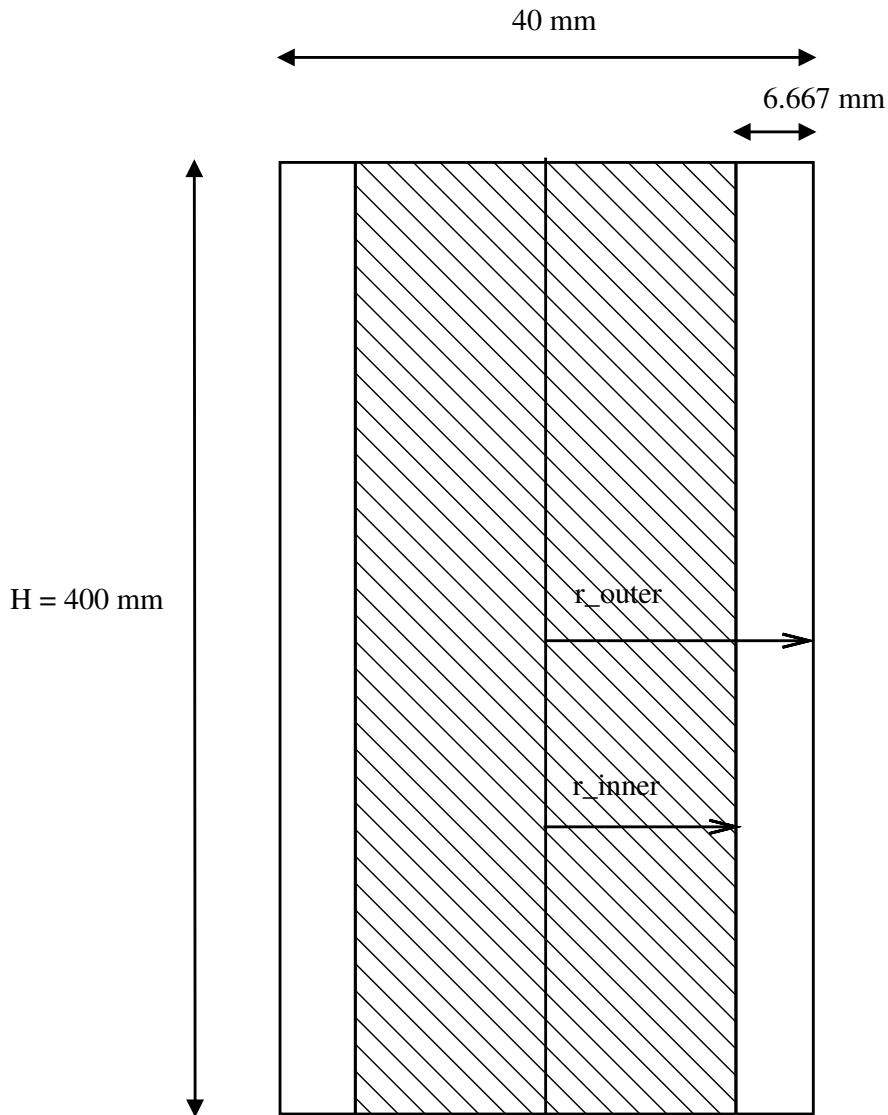


FIGURE 5: Schematic diagram of the vertical concentric cylinder used in this study

Table 3 presents properties of the water used as fluid in the annular gap between the two concentric cylinders. The values are taken from ANSYS' Material Library.

Correlations for both rectangular cavities and concentric cylinders were utilized for comparison. Rectangular cavities were included because the concentric cylinder was imagined "unrolled" into a long vertical rectangle (see Figure 6) with the side plates at different temperatures. The area of the walls in a concentric cylinder will however not be equal to each other, as the outer wall will have a larger area than the inner wall depending on the spacing of the annular gap between them. The correlations for rectangular boxes were therefore included out of interest to see how well this approximation agreed with the numerical solution or not at all.

| | Properties Water |
|------------------------|-----------------------|
| Density | 997 kg/m ³ |
| Molar Mass | 18.02 kg/kmol |
| Specific Heat Capacity | 4181.7 J/kg K |
| Dynamic Viscosity | 8.899E-04 kg/m s |
| Thermal conductivity | 0.6069 W/m K |
| Thermal Expansivity | 2.57E-04 1/K |

TABLE 3: Properties of water used in this study

MATLAB® R2013b, a high-level language for numerical computations, visualization and programming (MathWorks®, 2013), was utilized to solve the four empirical correlation equations (32), (34), (35) and (36) discussed in Section 3.1. The results are presented in Figures 7a and 7b. The subscripts "1", "2", "3" and "4" denotes the correlation equations (32), (34), (35) and (36), respectively.

Figure 7a shows that the four correlations predict heat transfer coefficients between 200-350 for a delta temperature of 46°C ($T_{inner} = 50^\circ\text{C}$), while approximately 260-420 for a delta temperature of 96°C ($T_{inner} = 100^\circ\text{C}$). The heat transfer coefficients h_1 and h_2 derived from the rectangular enclosure correlations, that is (32) and (34), predict lower values of heat transfer at the different temperatures tested, compared to h_3 and h_4 which were derived from cylindrical correlations ((35) and (36)). Based on the problem setup and correlations discussed in this study, Figure 7a implies that the buoyancy forces are predicted lower in enclosed rectangles than in vertical cylinders.

All of the correlations estimating Nusselt numbers predict increasing heat transfer coefficients with increasing temperature gradients, which is reasonable since h_1 , h_2 , h_3 and h_4 are based on the Nusselt number which is a measure of convection to conduction. If the wall temperature increases, the fluid close to the wall normally gets less dense and hence the free convection effects will increase as well, while the thermal conductivity of the fluid or material remains constant. The correlation from VDI-Wärmeatlas (2006) predicts highest heat transfer rates, and differ with approximately 25% down to h_3 from Hadjadj et al. (1999). It is worth mentioning that the correlation from Hadjadj et al. (1999) is based upon an open-ended vertical concentric cylinder, and may not predict accurate values for the problem in this study. The lowest heat transfer rates are predicted by Bejan (2013)'s theoretically derived correlations, followed by Rohsenow et al. (1998)'s correlation for vertical rectangular parallelepipeds. Between the values of h_1 and h_4 there are differences up to approximately 40%.

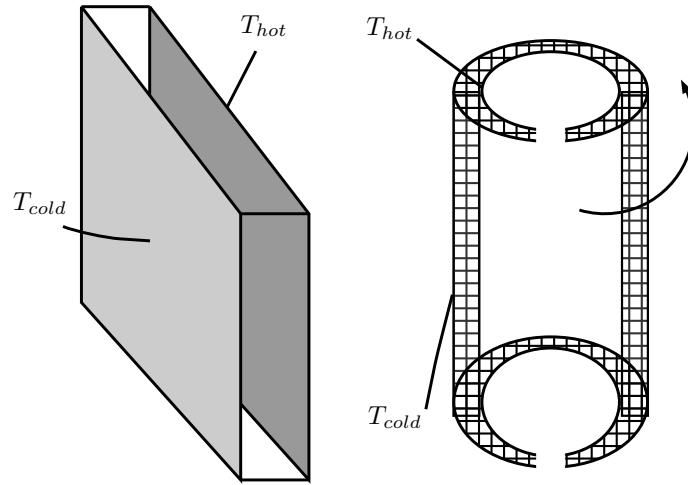
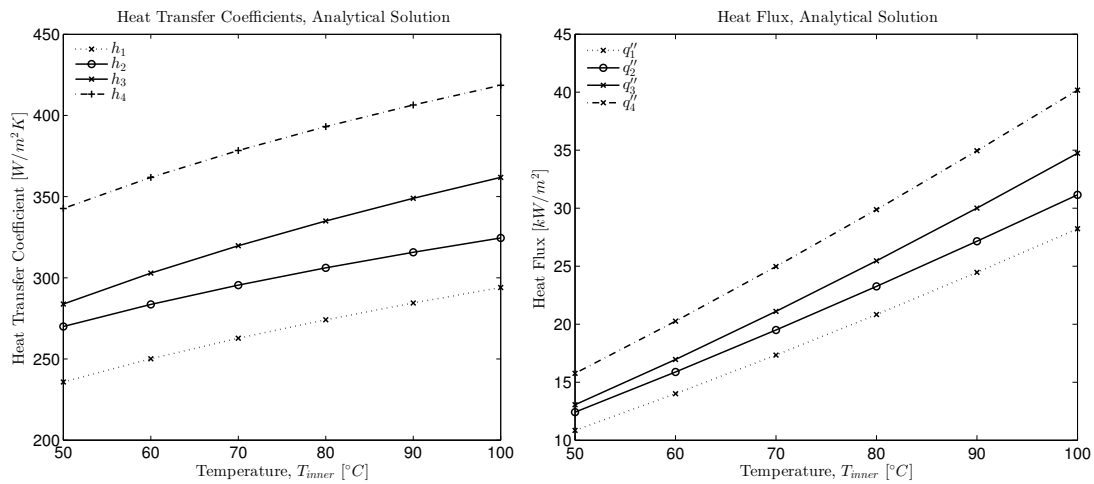


FIGURE 6: Illustration of the concentric cylinder being "unrolled"



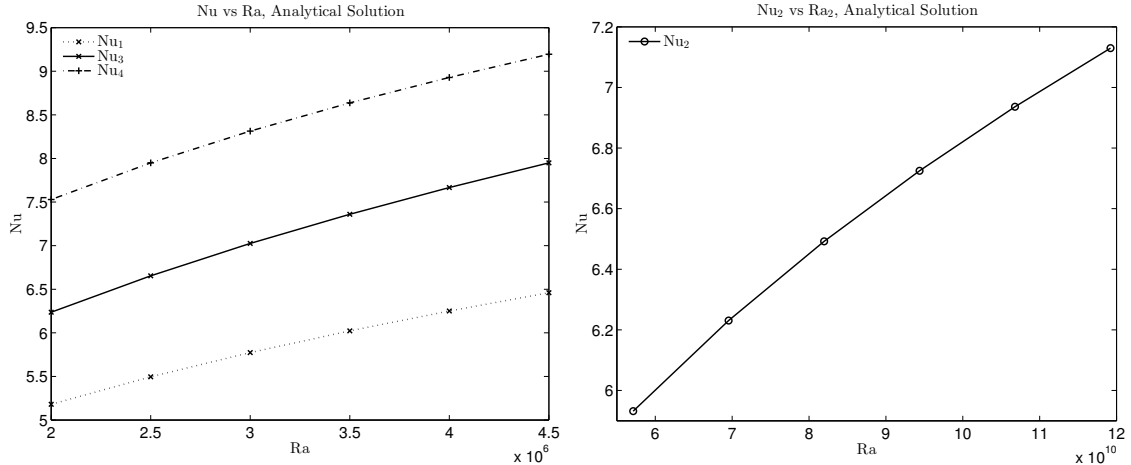
(A) Heat transfer coefficients occurring in the annulus predicted by the four correlations in the analytical solution (B) Heat flux occurring in the annulus predicted by the four correlations in the analytical solution versus the temperature of the inner cylinder

FIGURE 7: Heat transfer coefficients (7a) and heat flux 7b from the analytical solution

The graphs in Fig. 7b indicate heat fluxes ranging from 5 kW/m² - 16 kW/m² for the lowest temperature case computed, and up to 10 kW/m² - 35 kW/m² for the highest temperature case computed. As may be expected, the VDI-Wärmeatlas (2006) predicts the highest heat flux as its correlation yielded the highest heat transfer coefficient from Figure 7a.

The heat fluxes increase with increasing temperature differences, which is expected due to the driving force in free-convective heat transfer, which is based on buoyancy forces

and density gradients. When the wall temperature increases, the density of the fluid decreases and the buoyancy increases, resulting in an increasing driving force increasing the transportation of heat and thereby the heat flux.



(A) Nusselt number versus Rayleigh number for correlations equations (32), (34) and (36) (B) Nusselt number versus Rayleigh number for correlation equation (35)

FIGURE 8: Nusselt number versus Rayleigh number based on the analytical solution

Nu_1 , Nu_3 and Nu_4 versus the respective Rayleigh numbers, are presented in Figure 8a while Figure 8b shows the corresponding graph for Nu_2 . Ra_2 was based on the height H of the cavity as opposed to the three other correlations, and yielded therefore a Rayleigh number with a factor of 10^4 the other Rayleigh numbers. Eq. (32), (34) and (36) predict Nusselt numbers between approximately 5 - 7.5 for a temperature difference of 46°C ($Ra \approx 2 \times 10^6$) and between 6.5-9.2 for a temperature difference of 96°C ($Ra \approx 4.5 \times 10^6$). As may be expected from previous results (see Figure 7), VDI-Wärmeatlas (2006) predicts the highest Nusselt number, that is the highest heat transfer occurring due to convection, while Rohsenow et al. (1998) predicts the lowest Nusselt numbers for the given cases. The correlation form Bejan (2013) predicts Nusselt numbers ranging from approximately 5.9 ($Ra \approx 5.8 \times 10^{10}$) to 7.1 ($Ra \approx 12 \times 10^{10}$), ending up in between Nu_1 and Nu_3 , as expected due to the results seen in Figure 7. This is an example of different correlations being based on different characteristic dimensions.

It can be seen from Figure 8 that the Nusselt number increases with increasing Rayleigh numbers. The free convection effects increases because the buoyancy forces increase as a result of increasing temperatures, and by definition the Grashof number (and hence Rayleigh number, since $Ra = Gr \cdot Pr$, and Pr is dependent on the fluid only) will also increase simultaneously with the Nusselt number.

5 Numerical experiments

ANSYS® Workbench™ 2.0 Framework, version 15.0.0 was used to perform a CFD analysis of the free convection model. ANSYS® DesignModeler™ was used as CAD-tool for the modeling of the vertical concentric cylinder shown in Figure 5. The solver used for the thermal analysis was ANSYS CFX 15.0. Simulations were run with single precision in serial on a 64-bit Dell laptop, with Intel® Core™ i7 vPro™ 2.90 GHz Processors and 16 GB installed memory.

ANSYS CFX uses a coupled solver, which solves the mass and momentum equations as a single system by use of a fully implicit discretization of the equations at any given time step (ANSYS®, 2013). The time step is of importance, as it behaves like an acceleration parameter to guide the approximate solutions to a steady-state solution, given the problem type is steady-state, meaning the properties of the flow are not changing with time after reaching a certain value. This solution approach reduces the number of iterations required for convergence to steady-state, or to calculate the solution for each time step in a transient analysis (ANSYS®, 2013).

For comparison, both a 2D model and a 3D model were designed, modelled and tested. In this way, one could see if the 2D model gave an accurate enough solution with only one hundredth of the elements making up the 3D model. This would result in lower computational effort making the numerical experiments more efficient and less time consuming. The two models were run as both simplified models with the modified thermal conductivity k_{eff} based on the Nusselt number obtained from the analytical solution, as well as fully resolved models accounting for the free convection effects arising in the cavity when a temperature gradient is present. The wall temperatures were set in the boundary conditions in the setup provided by CFX-Pre.

5.1 Geometry: 2D and 3D

The geometries used in the thermal analysis were modelled in ANSYS® DesignModeler™. The characteristics of the models were the same as used in the analytical solution (see Section 4) and are presented in Table 2. The fluid located in the annular gap was water as for the analytical solution.

2D Model Being axisymmetrical, the concentric cylinder was highly relevant for being solved in 2D. It was modeled as a long rectangular surface as can be seen in Figure 9. ANSYS CFX operates only with three-dimensional spaces, so the surface had to be revolved 1° around the y-axis of the cylinder center, creating a small volume solvable in CFX.

The surface area of the 2D model was $A_s = 5569,3 \text{ mm}^2$ with a volume of $775,45 \text{ mm}^3$. The outer wall area was 139.6 mm^2 , while the inner wall area was 93.1 mm^2 .

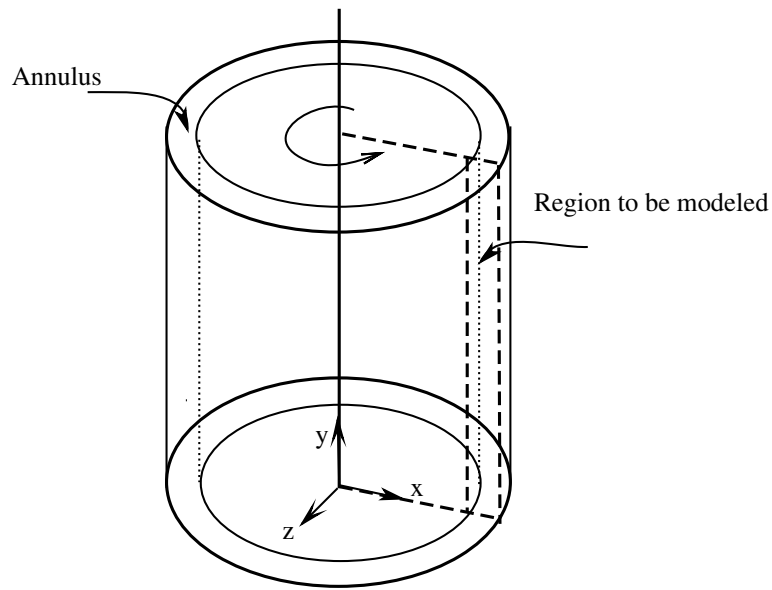


FIGURE 9: Illustration of the axisymmetrical concentric cylinder, with the 2D region that was modeled in ANSYS CFX

3D Model The 3D model was sketched as two circles with dimensions as shown in Table 2, and then extruded in the y-direction, leaving the core hollow since it was isothermal and did not require to be solved by CFX. The resulting surface area was $A_s = 85172 \text{ mm}^2$, making up a volume of $2.7925 \times 10^5 \text{ mm}^3$. The outer wall area was 50253.8 mm^2 whereas the inner area was 33502.5 mm^2 . The three-dimensional cylinder is pictured in Figure 10.

5.2 Cases

The cases presented in Table 4 were considered and simulated for each inner temperature $T_i = 50, 60, 70, 80, 90$ and 100°C , with the constant outer wall temperature $T_o = 4^\circ\text{C}$. The table shows that the heat transfer for the simplified model occurs through conduction with an effective thermal conductivity k_{eff} [W/m K] of the material, while the fully resolved model is based on convective heat transfer by means of a heat transfer coefficient h [W/m² K].

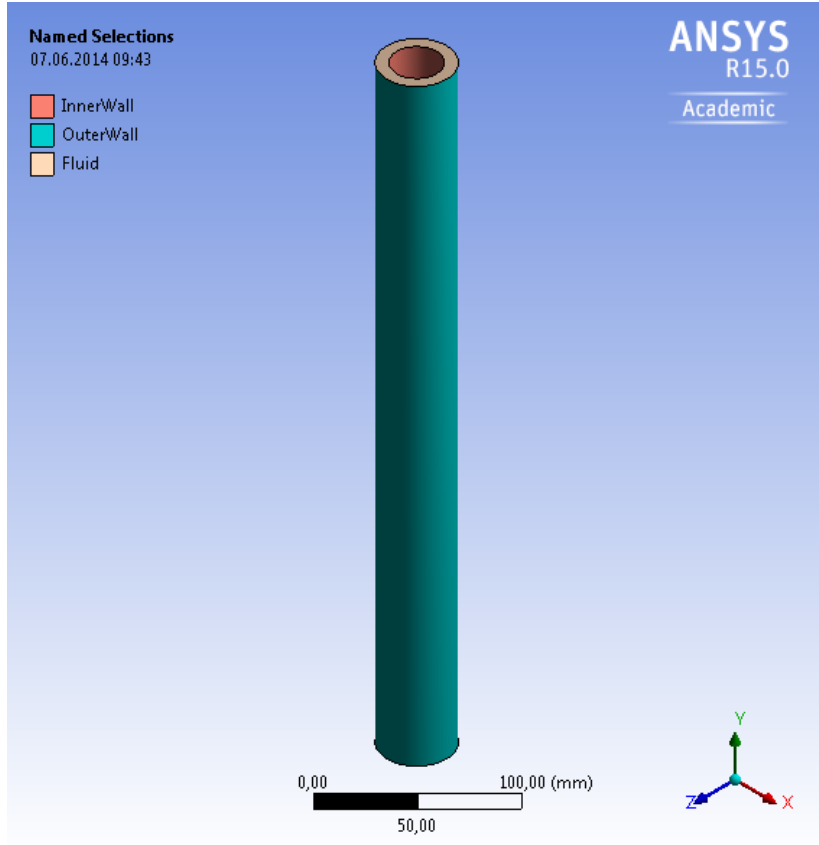


FIGURE 10: The 3D model showing the inner and outer cylinder wall with the fluid located in the annulus

| | 2D | | 3D | |
|-------|--------------------|----------------|--------------------|----------------|
| T | Simplified | Fully resolved | Simplified | Fully resolved |
| T_i | k_{eff_1} | | k_{eff_1} | |
| | k_{eff_2} | h | k_{eff_2} | h |
| | k_{eff_3} | | k_{eff_3} | |
| | k_{eff_4} | | k_{eff_4} | |

TABLE 4: Cases that were considered numerically for $T_i = 50 - 100^\circ\text{C}$. The effective thermal conductivity values, k_{eff} [W/m K], were calculated in the analytical solution in Section 4, while k_{water} is the thermal conductivity of water.

Table 4 shows that for each delta temperature tested, there were four simplified models obtained from the four correlations in Eq. (32), (34), (35) and (36), and one fully resolved model. This related to both the 2D and 3D model, making up a total number of 60 simulations.

5.2.1 Simplified Model with Modified Thermal Conductivity

For the simplified model, it was assumed that the fluid in the annulus thermally behaved similar to a solid with a modified thermal conductivity. An effective thermal conductivity was used for this purpose, based on the properties of water presented in Table 3, and the Nusselt numbers obtained from the empirical correlations used in the analytical solution (Section 4) of the free convection problem. The effective thermal conductivity was defined as

$$k_{\text{eff}} = \text{Nu} \cdot k \quad (40)$$

The domain of interest was set to be solid in CFX-Pre, and the user-defined material was defined with the same properties as water (see Table 3), but with k_{eff} substituted with k_{water} .

Looking at Eq. (40), it can be seen that it implies $k_{\text{eff}} > k$ for $\text{Nu} > 1$, that is when the convective heat transfer is larger than the conductive heat transfer. This is due to the fact that when looking at simplifications, certain properties have to be modified so the real life situation can be better reflected and the results more trustworthy. In this case, the effective thermal conductivity has to account for the buoyancy effects that will dominate and govern the actual free convection problem. The computed effective thermal conductivities for each case and each correlation equation is presented in Table 5. Simulations were run with k_{eff} [W/m K] for each T_i [°C], both for the 2D and 3D models.

| T_i | Eq. (32) | | Eq. (34) | | Eq. (35) | | Eq. (36) | |
|-------|---------------|--------------------|---------------|--------------------|---------------|--------------------|---------------|--------------------|
| | Nu_1 | k_{eff_1} | Nu_2 | k_{eff_2} | Nu_3 | k_{eff_3} | Nu_4 | k_{eff_4} |
| 50 | 5.1805 | 3.1440 | 5.9318 | 3.6000 | 6.2360 | 3.7847 | 7.5287 | 4.5692 |
| 60 | 5.4954 | 3.3352 | 6.2308 | 3.7815 | 6.6543 | 4.0385 | 7.9491 | 4.8243 |
| 70 | 5.7731 | 3.5037 | 6.4921 | 3.9400 | 7.0250 | 4.2635 | 8.3138 | 5.0456 |
| 80 | 6.0226 | 3.6551 | 6.7251 | 4.0815 | 7.3598 | 4.4667 | 8.6373 | 5.2420 |
| 90 | 6.2502 | 3.7932 | 6.9362 | 4.2096 | 7.6663 | 4.6527 | 8.9289 | 5.4190 |
| 100 | 6.4599 | 3.9205 | 7.1296 | 4.3269 | 7.9497 | 4.8246 | 9.1952 | 5.5806 |

TABLE 5: The effective thermal conductivity and Nusselt number based on the correlation equations in the analytical solution

5.2.2 Fully Resolved Model

The fully resolved model was taking into account the actual buoyancy forces that will develop in the cavity in a real life situation due to different wall temperatures, and which will be the driving force for fluid motion and hence heat transfer. Although the trapped

fluid in real life situations will not only be compounded of pure water but also other substances such as saline water and glycols for instance, only pure water as found in ANSYS' material library was used to model the free convection effects due to simplicity.

5.3 Grid Description

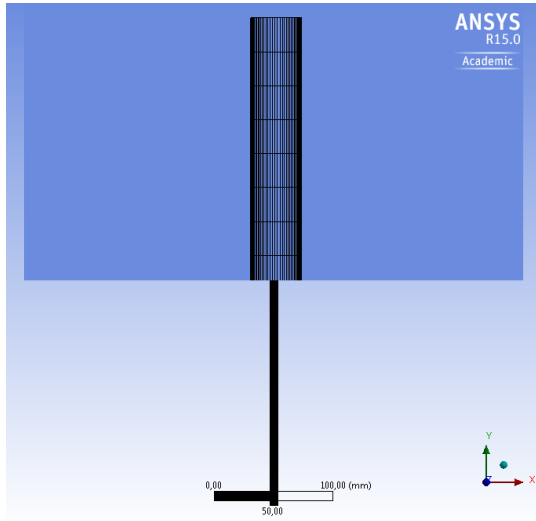
ANSYS CFX uses finite volumes constructed by the grid to derive a solution to the numerical problem. The spatial domain is discretized by the grid and the solution will depend on the grid method and refinement. Control volumes around the nodes are used to ensure conservation of the relevant quantities that are to be solved, such as mass, momentum and energy components. CFX stores the solution variables and fluid properties at the mesh vertices.

Structured grids were generated for both the 2D and 3D models in ANSYS® Meshing™.

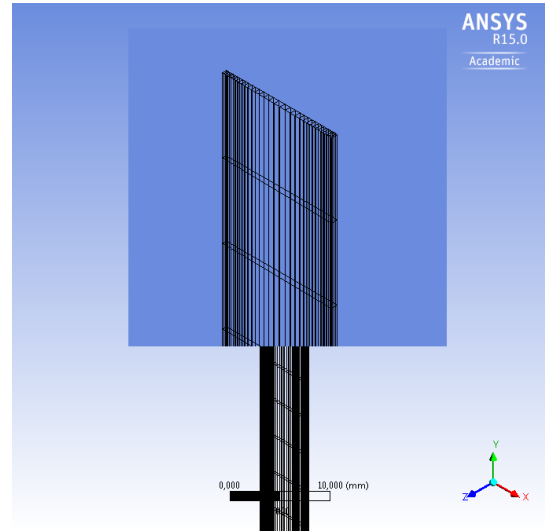
Grid description: 2D A sweeping method was used to generate quadrangle elements for the 2D model, together with both vertical and horizontal edge sizing-methods to adjust the number of volume elements. The model was swept from the upper wall of the cavity to the lower wall. The 2D grid is pictured in Figure 11.

| | Coarse grid | Medium grid | Fine grid |
|-------------------------|-------------|-------------|-----------|
| Number of elements | 1,500 | 2,100 | 3,150 |
| Number of nodes | 3,162 | 4,402 | 6,552 |
| Mesh method | Sweep | Sweep | Sweep |
| Free mesh type | All quad | All quad | All quad |
| Edge sizing, vertical | 50 | 70 | 90 |
| Edge sizing, horizontal | 20 | 30 | 35 |
| Element size [mm] | 0.33 | 0.22 | 0.19 |

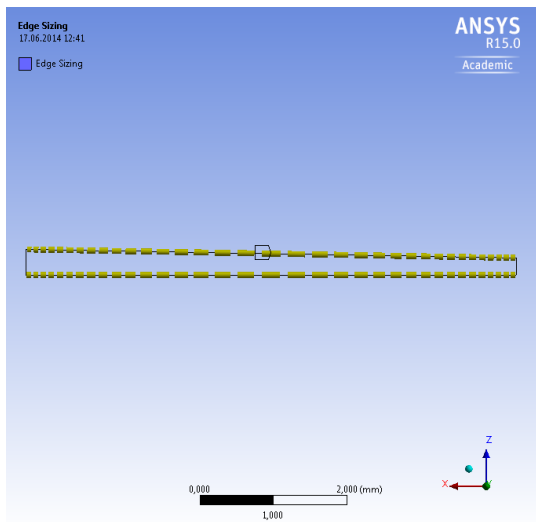
TABLE 6: Grid properties for the coarse, medium and fine 2D grids



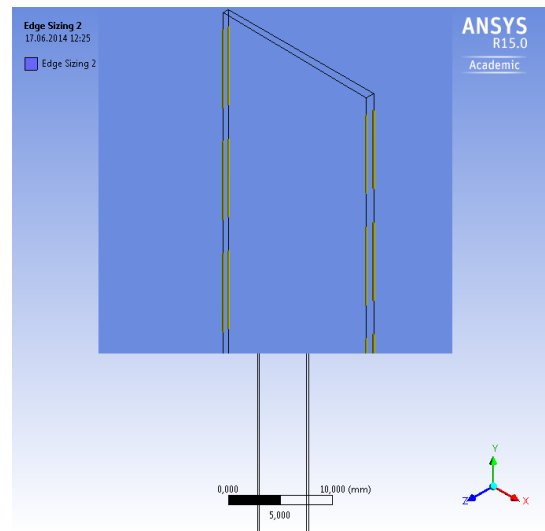
(A) 2D-grid seen from the front



(B) 2D-grid, ISO-view



(C) Edge sizing across the annulus



(D) Edge sizing along the vertical walls

FIGURE 11: The 2D grid with the element spacing decreasing towards the vertical cylinder walls

Grid Description: 3D For the 3D model, a MultiZone method was used to create a mapped mesh of hexahedra elements. The method was then inflated on the inner and outer walls of the concentric cylinder, that is the vertical walls exposed to different temperatures. Maximum inflation layers used were 10, with a growth rate of 1.5. The transition was set to be smooth with a ratio of 0.1. The 3D mesh is shown in Figure 12.

| | Coarse grid | Medium grid | Fine grid |
|--------------------|-------------------|-------------------|-------------------|
| Number of elements | 144,000 | 538,272 | 832,000 |
| Number of nodes | 129,712 | 562,800 | 867,984 |
| Mesh method | MultiZone | MultiZone | MultiZone |
| Mapped mesh type | Hexa | Hexa | Hexa |
| Element size [mm] | 3.00 | 1.50 | 1.25 |
| Inflation option | Smooth Transition | Smooth Transition | Smooth Transition |
| Transition ratio | 0.1 | 0.1 | 0.1 |
| Maximum layers | 10 | 10 | 10 |
| Growth rate | 1.5 | 1.5 | 1.5 |

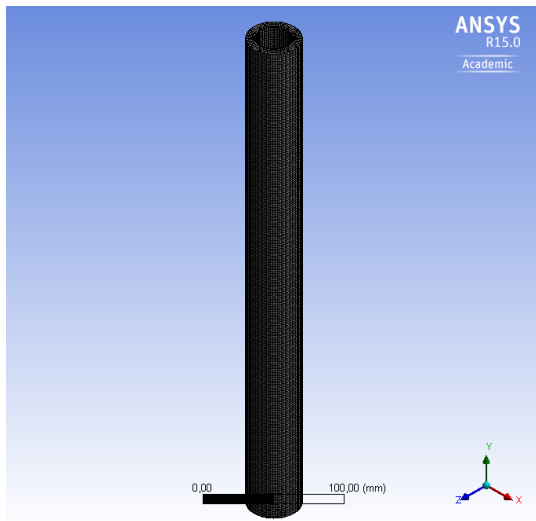
TABLE 7: Properties of the coarse, medium and fine 3D grids

5.4 Boundary Conditions

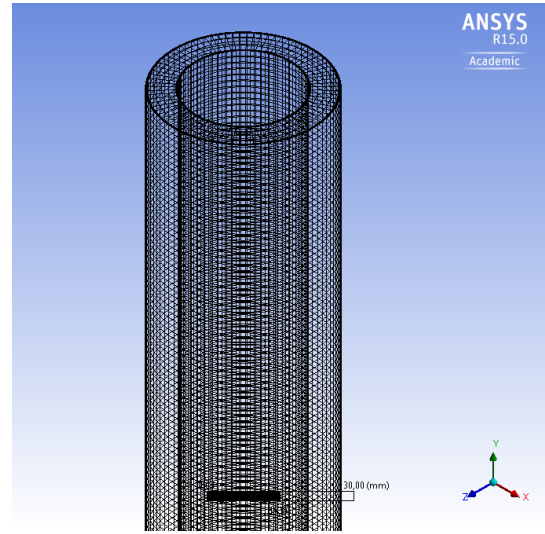
The model boundaries were split in four sections with regards to the boundary conditions. The vertical walls of the cylindrical cavity were set to be isothermal with a no-slip condition implying the fluid velocity in the layer closest to the wall is zero (due to friction). Upper and lower boundaries of the enclosure were set to be adiabatic walls with a free-slip condition (no friction). An adiabatic boundary condition corresponds to the walls being insulated. For the axisymmetric case, the two additional vertical surfaces connecting the inner and outer walls were set to be symmetrical. Table 8 lists the boundary conditions used in this study, and applies to all of the cases.

| | Boundary Condition |
|-------------|------------------------|
| Inner Wall | Isothermal, T_{hot} |
| | No-slip, smooth wall |
| Outer Wall | Isothermal, T_{cold} |
| | No-slip, smooth wall |
| Top Wall | Adiabatic |
| | Free-slip |
| Bottom wall | Adiabatic |
| | Free-slip |

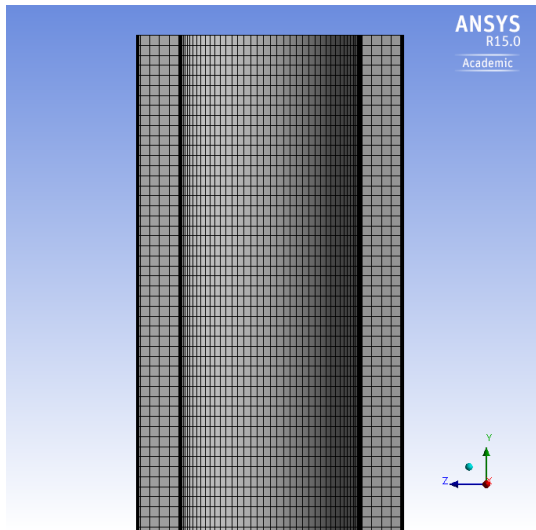
TABLE 8: Boundary conditions for the concentric cylinder used in the numerical experiments



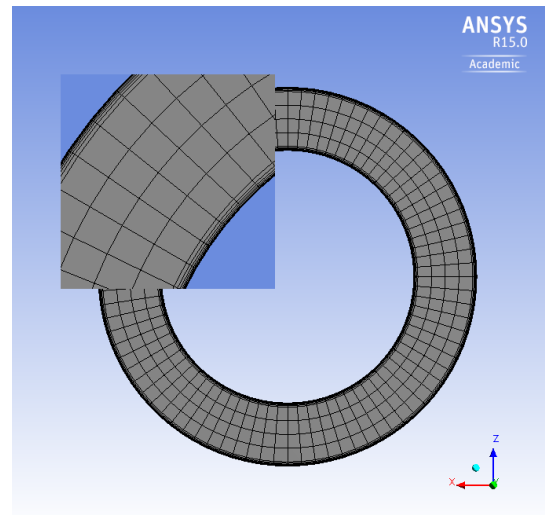
(A) Overview of the 3D grid



(B) The upper part of the cylinder showing the 3D grid



(C) The 3D grid at a section plane going straight through the cylinder



(D) The cylinder seen from the top

FIGURE 12: The 3D grid with inflation layers close to the vertical walls

5.5 Numerical Model

Based on the results from the analytical solution in Section 4, the Rayleigh number was assumed to exceed 1×10^6 . According to Rohsenow et al. (1998), these values for Ra correspond to turbulent flow for the relevant aspect ratios dealt with in this study. Based on this assumption, a turbulence model was decided on to solve the governing equations discussed in Section 2.3.

Very often time-averaged properties of fluid motion give sufficient information about

the turbulent behaviour of the flow (Versteeg and Malalasekera, 1995), because turbulent flow tend to exhibit average characteristics when looking at large enough time scales. In addition, a time-varying, fluctuating component will also be present in the turbulent flow together with the averaged properties (ANSYS® , 2013). When time-averaged properties are introduced to the governing equations, that is the Navier-Stokes equations, a newborn set of equations called Reynolds-Averaged Navier-Stokes (RANS) equations come to live. ANSYS utilizes these RANS equations, in combination with an optional turbulence model. The turbulence model takes care of the extra turbulent stresses, the so called Reynolds stresses $\rho \overline{u'_i u'_j}$, which appear from time-averaging the Navier-Stokes equations to account for turbulent fluctuations in fluid momentum (Versteeg and Malalasekera, 1995).

The RANS-based two-equation turbulence model $k-\omega$ was chosen as numerical model. This model is known for its near-wall treatment for low Reynolds number computations (ANSYS® , 2013), and in free convective heat transfer, the Reynolds number is very low compared to forced convection. The $k-\omega$ model offers two transport equations for the turbulent fluctuating components in the fluid flow, where k represents the turbulent kinetic energy, while ω represents the specific dissipation. The first one determines the energy in the flow, while the latter determines the scale of the turbulence (ANSYS® , 2013). The $k-\omega$ model is categorized under linear eddy viscosity models, meaning that the Reynolds stresses are modeled by the linear relationship after the Boussinesq approximation discussed in Section 2.3.2. The Boussinesq model in CFX uses a constant density fluid model, but applies a local gravitational body force throughout the fluid where the mentioned linear relationship is established between the thermal expansivity coefficient β and the local temperature difference (ANSYS® , 2013).

The buoyancy model in CFX-Pre was activated, meaning a constant reference density ρ_{ref} was used for all terms in the RANS equations other than the buoyancy source term that is added to the momentum equation. The buoyancy reference temperature was set to 25°C and the reference pressure to 1 atm. The gravity force was set equal to -9.81 m/s² in the y-direction, while 0 m/s² in both the x- and z-directions.

The $k-\omega$ model is said to be more accurate and robust than other turbulence models as for instance the $k-\epsilon$ model, where complex damping functions can be added in an attempt to handle low Reynolds number flows and which may lead to instability (ANSYS® , 2013). Every turbulence model comes with advantages and disadvantages, and in CFD it comes down to the configuration of the problem under investigation which model is more suitable than the others to that specific problem. When $k-\omega$ -based models are applied in CFX, an Automatic near-wall treatment method comes along, which is a near wall boundary condition developed by CFX to allow for a smooth shift from a low-Reynolds number form to a wall function formulation near the wall.

The analysis was run as steady state.

5.5.1 Heat Flux in the Near-Wall Region

The non-dimensional near-wall temperature, T^+ , is defined by ANSYS as:

$$T^+ = \frac{\rho c_p u^* (T_w - T_f)}{q_w} \quad (41)$$

where T_w is the temperature at the wall, u^* is the logarithmic velocity, T_f the fluid temperature, c_p the fluid heat capacity and q_w the heat flux at the wall. When the wall temperature T_w is known, as in this case, the energy balance for each control volume can be obtained by rearrange the equation for T^+ :

$$q_w = \frac{\rho c_p u^*}{T^+} (T_w - T_f) \quad (42)$$

The wall heat flux is computed from the equation above, and then multiplied by the surface area and added to the boundary energy control volume equation (ANSYS®[®], 2013). When the wall boundary is fixed at a specified temperature T_w , that is the wall is isothermal, the heat flux for turbulent flow into the domain is by default considered by CFX as

$$q_W = h_c(T_W - T_{nW}), \quad (43)$$

where T_{nW} is the near-wall temperature and h_c is the wall heat transfer coefficient estimated based on the turbulent wall functions (ANSYS®[®], 2013).

5.6 Discretization Schemes

Solving partial differential equations on computers requires a finite amount of data. When dealing with continuous equations, a method to turn the equations into finite equations solvable for a computer is needed. This process is referred to as *discretization*, and yields an approximation to the exact solution one would obtained with an infinitely large number of computational cells. There are different discretization schemes available for different problems, which may be significant when looking at convection problems. The principal problem in discretization of convective terms represented in a heat flux balance in a control volume, is the calculation of the transported properties at the control volume faces and the convective flux across these boundaries (Versteeg and Malalasekera, 1995).

A **High Resolution** advection scheme of first order accuracy was used in the numerical experiments performed in this study, to achieve high accuracy.

5.7 Grid Independence

5.7.1 Convergence Control

A convergence level of 1×10^4 is normally sufficient for many CFD simulations, and was chosen for the root mean square (RMS) normalized residuals as a starting point for the iterations in CFX-Solver Manager. A tighter convergence criteria may be recommended for thermal analyses of subsea equipment, due to the importance of accurate predictions related to the huge production volumes and heat transfer involved.

A physical timescale of 0.01 seconds was primarily used for the timescale control, although simulations with a timescale of 0.001 seconds also were run for comparison. The latter proved to converge steady, but at a very slow rate. This is pictured in the convergence history plots for the 3D medium mesh model in Figure 15, where one can see that a physical timescale of 0.001 seconds required approximately 8000 iterations to reach the same convergence level as a physical timescale of 0.01 seconds did after only 1000 iterations.

Figure 13 shows the convergence history for the 2D fine mesh. The temperature at point (0.036, 0.2, 0) in the center of the model was monitored and reached a steady value of 304.26 K ($\sim 31.1^\circ\text{C}$) after 4000 iterations. The overall imbalance for the governing equations (see Figure 13d) lay between 0-0.547.

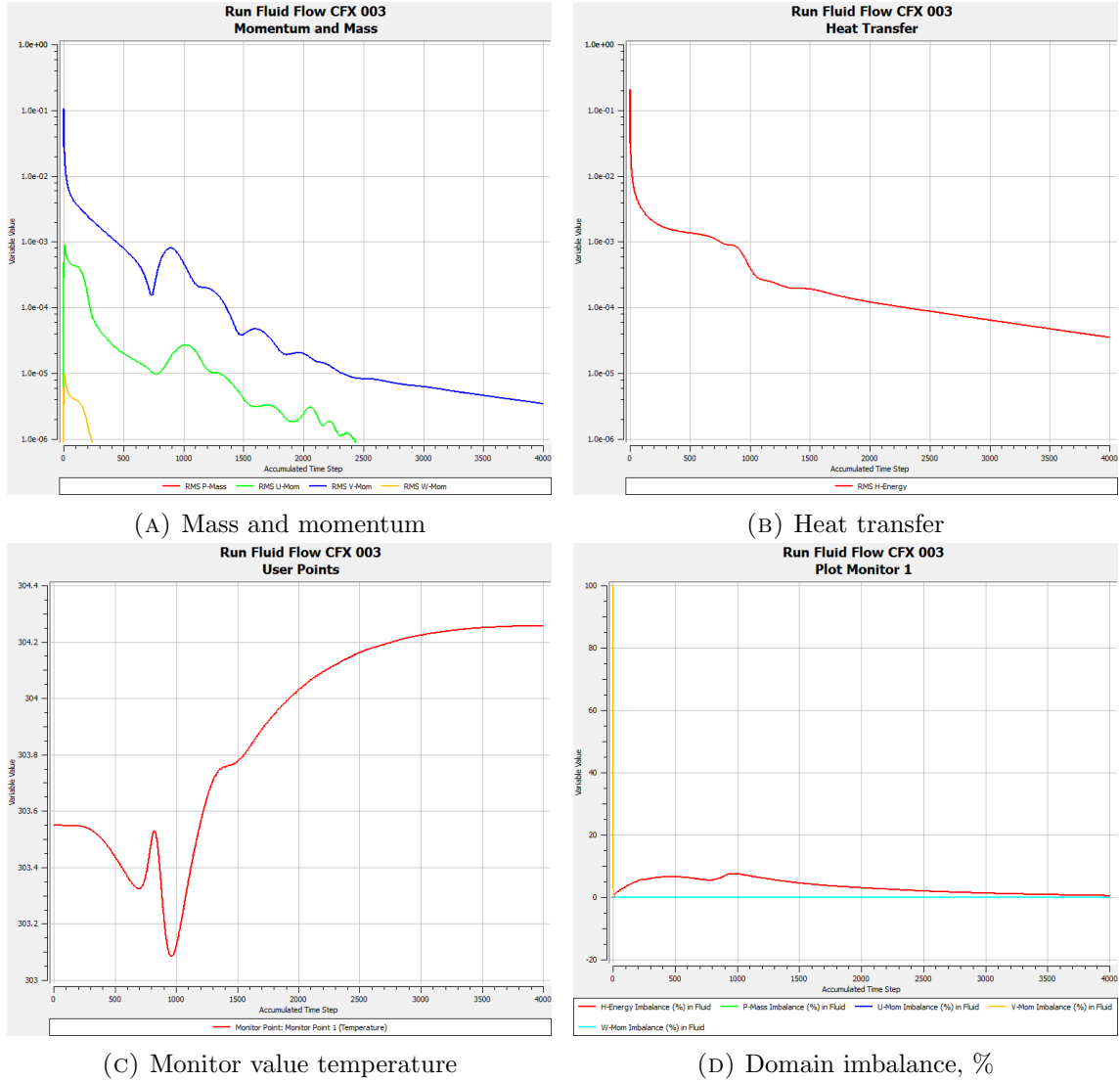
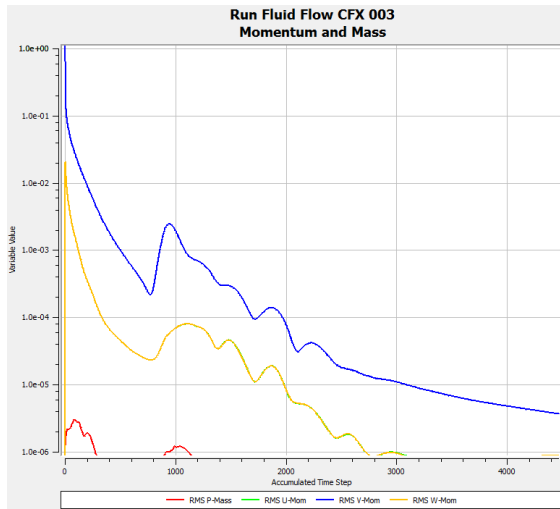
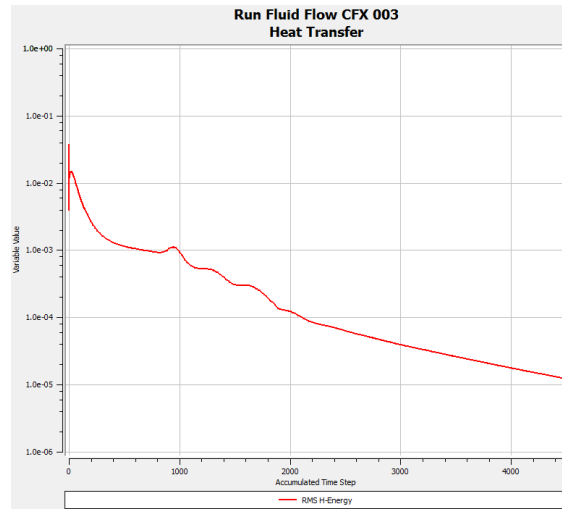


FIGURE 13: Convergence history for the fine 2D grid

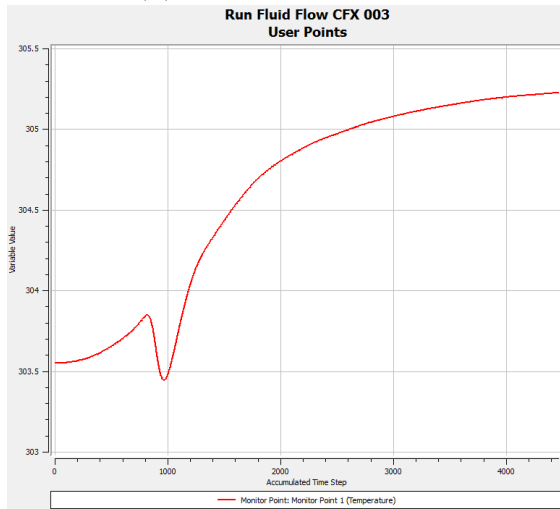
Figure 14 shows the convergence history for the 3D medium mesh. The temperature at point (0.016, 0.2, 0) in the center of the model was monitored and reached a steady value of 305.23 K ($\sim 32.1^\circ\text{C}$) after 4500 iterations. The overall imbalance for the governing equations (see Figure 14d) lay between 0-0.876.



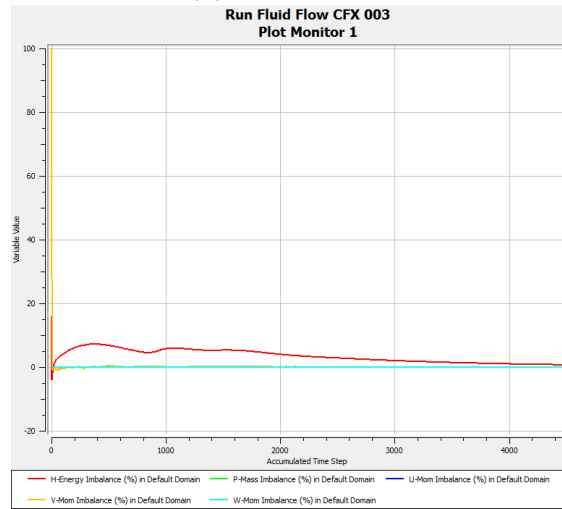
(A) Mass and momentum



(B) Heat transfer

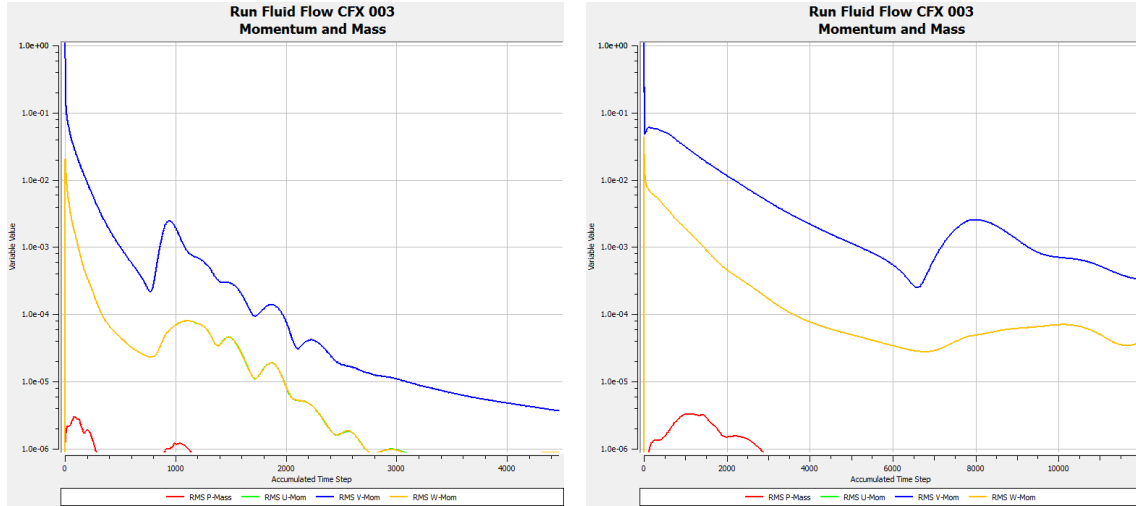


(C) Monitor value temperature



(D) Domain imbalance, %

FIGURE 14: Convergence history for the medium 3D grid



(A) Convergence history for the medium 3D grid for a physical timestep of 0.01

(B) Convergence history for the medium 3D grid for a physical timestep of 0.001

FIGURE 15: Comparison between the physical timesteps 0.01 seconds (15a) and 0.001 seconds (15b)

5.7.2 Grid Refinement

When working with computational fluid dynamics, it is important that the solution is independent of the mesh resolution to gain confidence in the results and also to know if the results are reliable. The solution will be a numerical solution to the problem based on the mesh and boundary conditions, and its accurateness will depend on the accuracy of the mesh and boundary conditions. The solution has to be tested, to see if the grid refinement meets the requirements. If a fine and a coarse mesh approximately yield the same monitored values, mesh independence is said to be achieved and one should do further simulations with the coarse mesh if the study require many simulations, due to less computational effort.

Monitor points were used to see how the temperature at a point in the center of the 2D and 3D cavities varied with each iteration when the inner wall temperature was 70°C. The monitored temperature values were then compared to see if grid independence was reached. The results are presented in Table 9.

| Grid | 2D | | | 3D | | |
|-------------------------------|----------|----------|----------|----------|----------|----------|
| | 1 | 2 | 3 | 4 | 5 | 6 |
| Elements | 1,500 | 2,100 | 3,150 | 144,000 | 538,272 | 832,000 |
| Run time (2000 iterations) | 00:03:12 | 00:03:46 | 00:05:09 | 01:57:23 | 07:11:30 | 11:52:15 |
| Temperature [K] | 304.15 | 304.23 | 304.26 | 303.96 | 305.23 | 305.94 |
| Deviation from Grid 6 [%] | 0.59 | 0.56 | 0.55 | 0.60 | 0.23 | 0.00 |

TABLE 9: Grid independence study

Table 9 shows that simulations with the three different 2D grids ran 2000 iterations quite fast compared to the 3D-simulations. Given the insignificant extra seconds it took to run the fine mesh of the 2D model, Grid 3 was chosen for further simulations due to faster convergence rate compared to Grid 1 and 2.

The coarse 3D mesh was considered inadequate compared to the finer grids, due to its convergence history that can be seen in Figure 16 and its temperature value in Table 9. Grid 5, the medium 3D mesh, resulted in a temperature value of 305.23 K, which only differed from the finer 3D grid with 0.2%. Grid 5 was concluded sufficient relative to the finer mesh (Grid 6), and was chosen for further simulations.

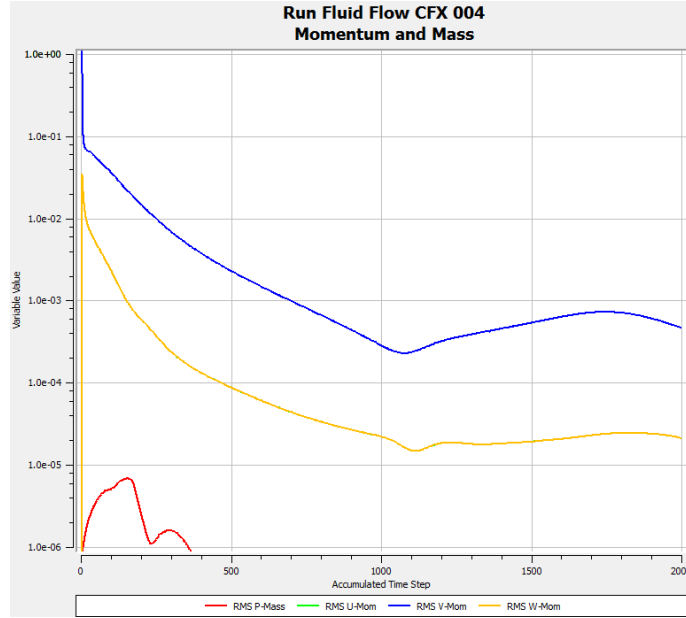


FIGURE 16: Convergence history coarse 3D mesh

6 Results

6.1 Simplified Model

The simplified model was based on the effective thermal conductivity estimated from the four correlations in Section 4 and computed by Eq. (40). Since the domain was modeled as solid, the heat transfer was through conduction only and the solution converged after few iterations with a convergence level of the residuals of 1×10^{-5} .

Figure 17 shows the temperature contour for the simplified 2D model simulated with $T_i = 70^\circ\text{C}$ and $T_o = 4^\circ\text{C}$. As expected, the temperature distribution is similar along the x -direction for every y throughout the cavity.

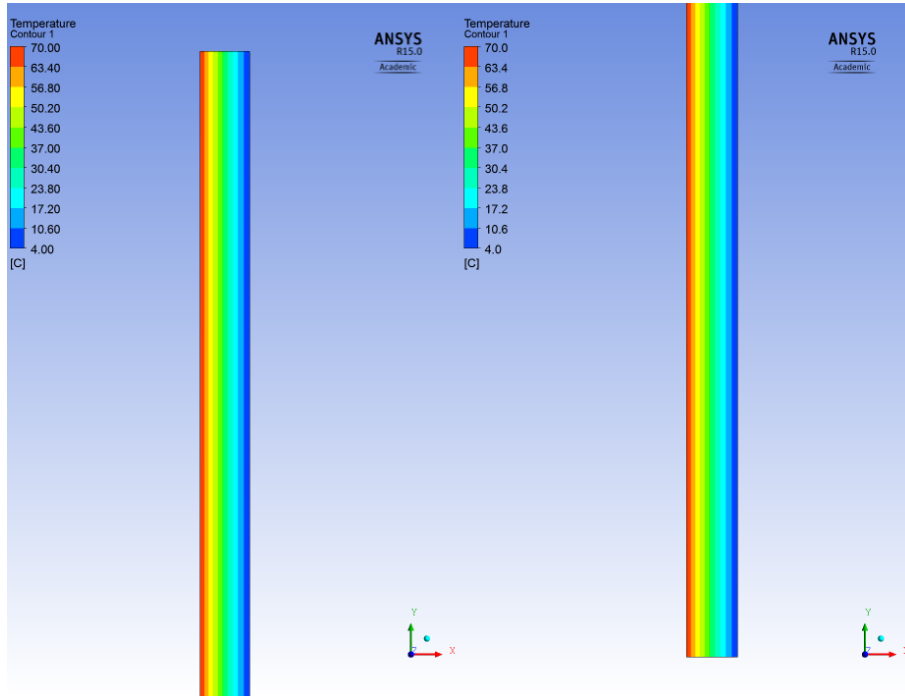


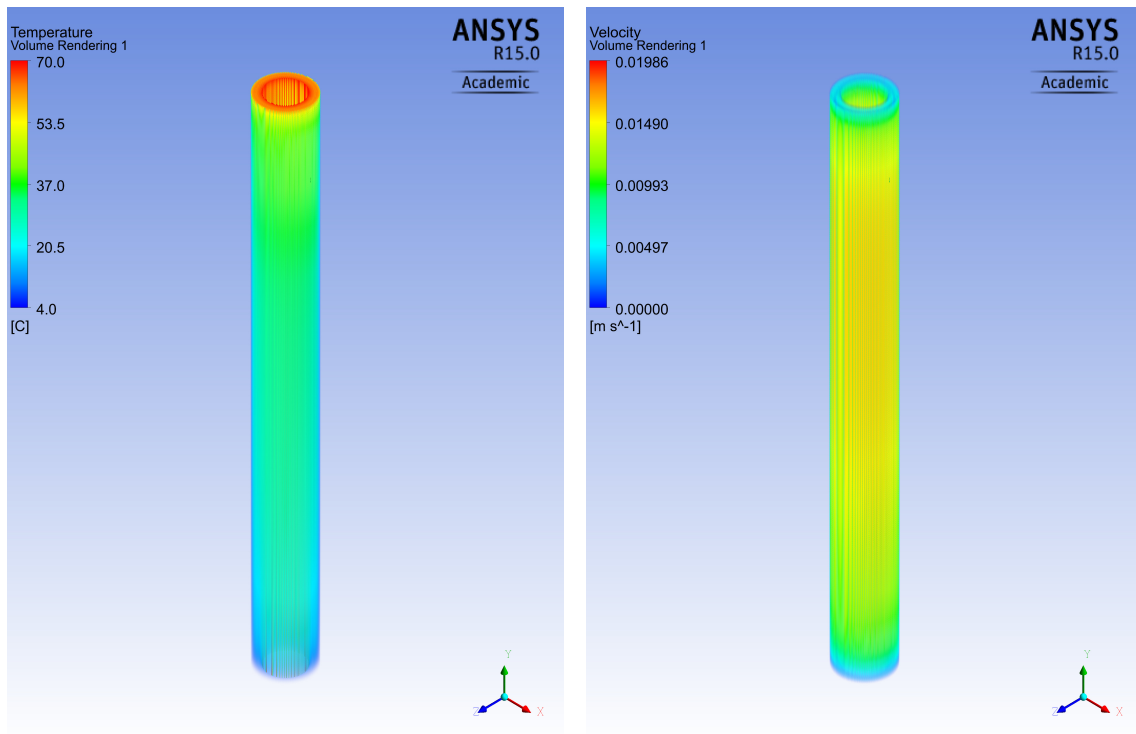
FIGURE 17: Temperature contour for the simplified model with the inner wall being 70°C

6.2 Fully Resolved Model

The heat flux and heat transfer coefficients obtained from simulations with the fully resolved 2D and 3D models are presented in Table A3 and A4.

Figure 18 shows the temperature distribution as well as the velocity distribution of the trapped fluid. Figure 18a shows the temperature distribution for $T_i = 70^\circ\text{C}$ and the constant $T_o = 4^\circ\text{C}$, acting as expected - the warmer and less dense fluid flow upwards due to buoyancy forces, while the colder and more dense fluid sinks to the bottom due to gravity forces. Figure 18b shows that the fluid is less active at the top and bottom of

the cavity, which is expected since these walls are adiabatic and the fluid is sort of at rest here, meaning the top and bottom will not influence the fluid dramatically.



(A) Temperature distribution in the concentric cylinder

(B) Velocity distribution in the concentric cylinder

FIGURE 18: Temperature (18a) and velocity (18b) distribution with the inner wall being 70°C

The temperature contours of the 2D and 3D fully resolved models are shown in Figure 19 and 20. One observation was that the fluid temperature appeared more distributed in the 3D model compared to the 2D model. This may be due to the 3D model being able to capture the turbulence and circulations better than the thin 2D model.

Both models predict a high-temperature region at the top of the cavity with a low-temperature region at the bottom, as expected with free convective heat transfer. Figure 20 shows the symmetry condition occurring in cylinders.

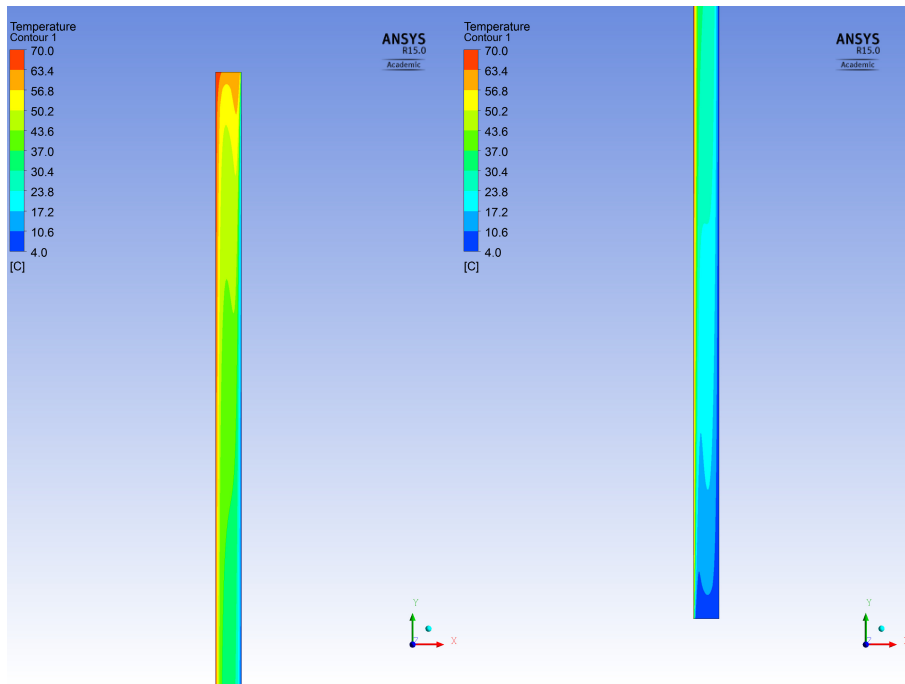


FIGURE 19: Temperature contour for the fully resolved 2D model

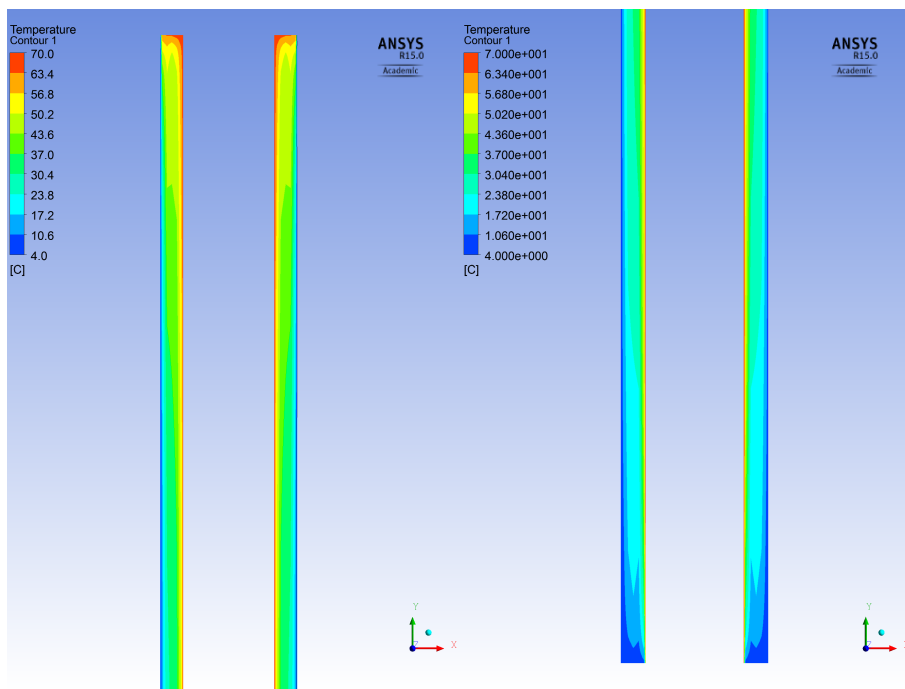


FIGURE 20: Temperature contour for the fully resolved 3D model

From Figure 21 one see that the 2D model only predicts one big section of circulation, instead of several circulation sections along the y-direction. This applies also to the 3D model in Figure 22.

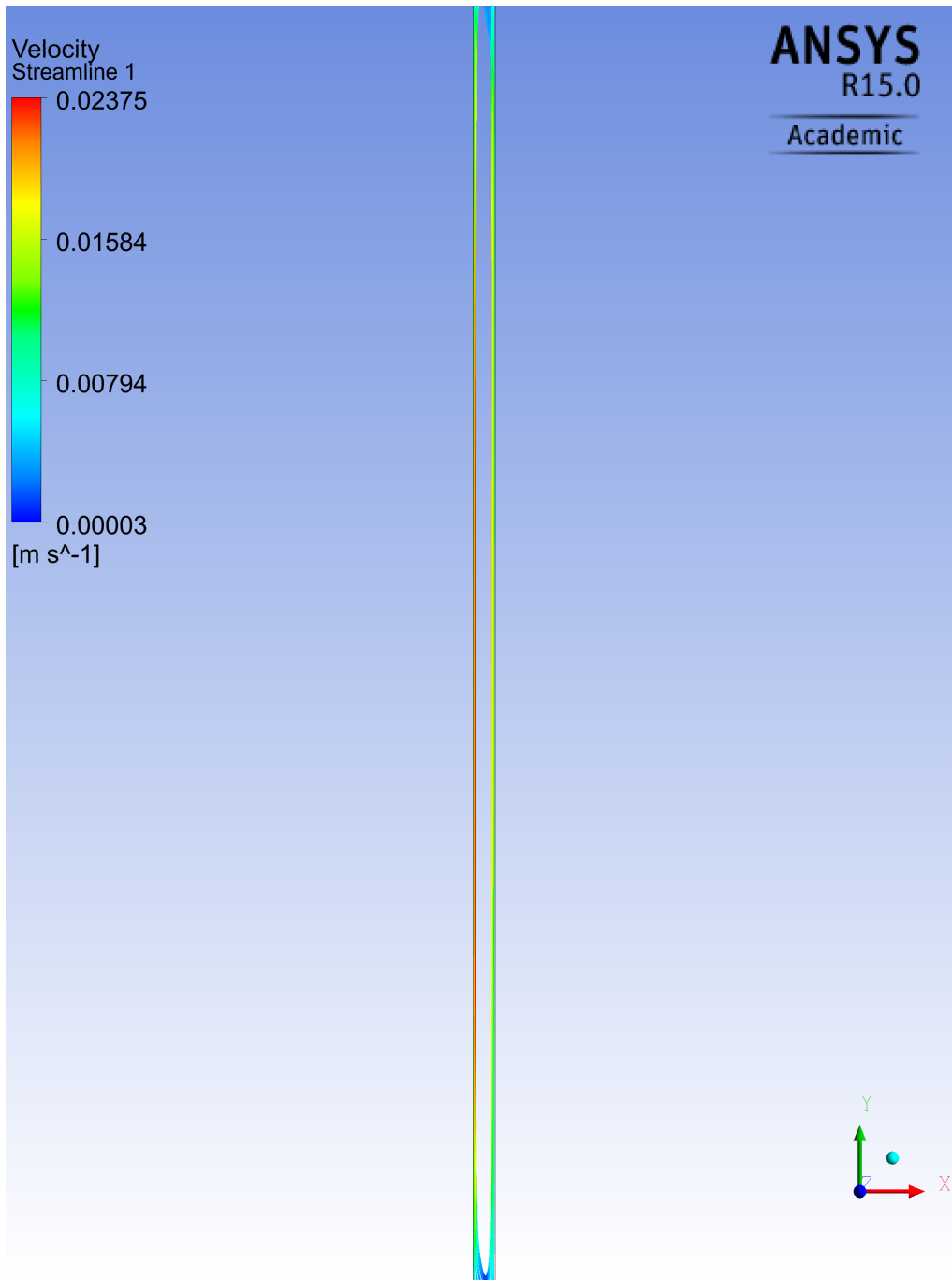


FIGURE 21: Streamlines from the 2D model, showing the circulation occurring in the cavity

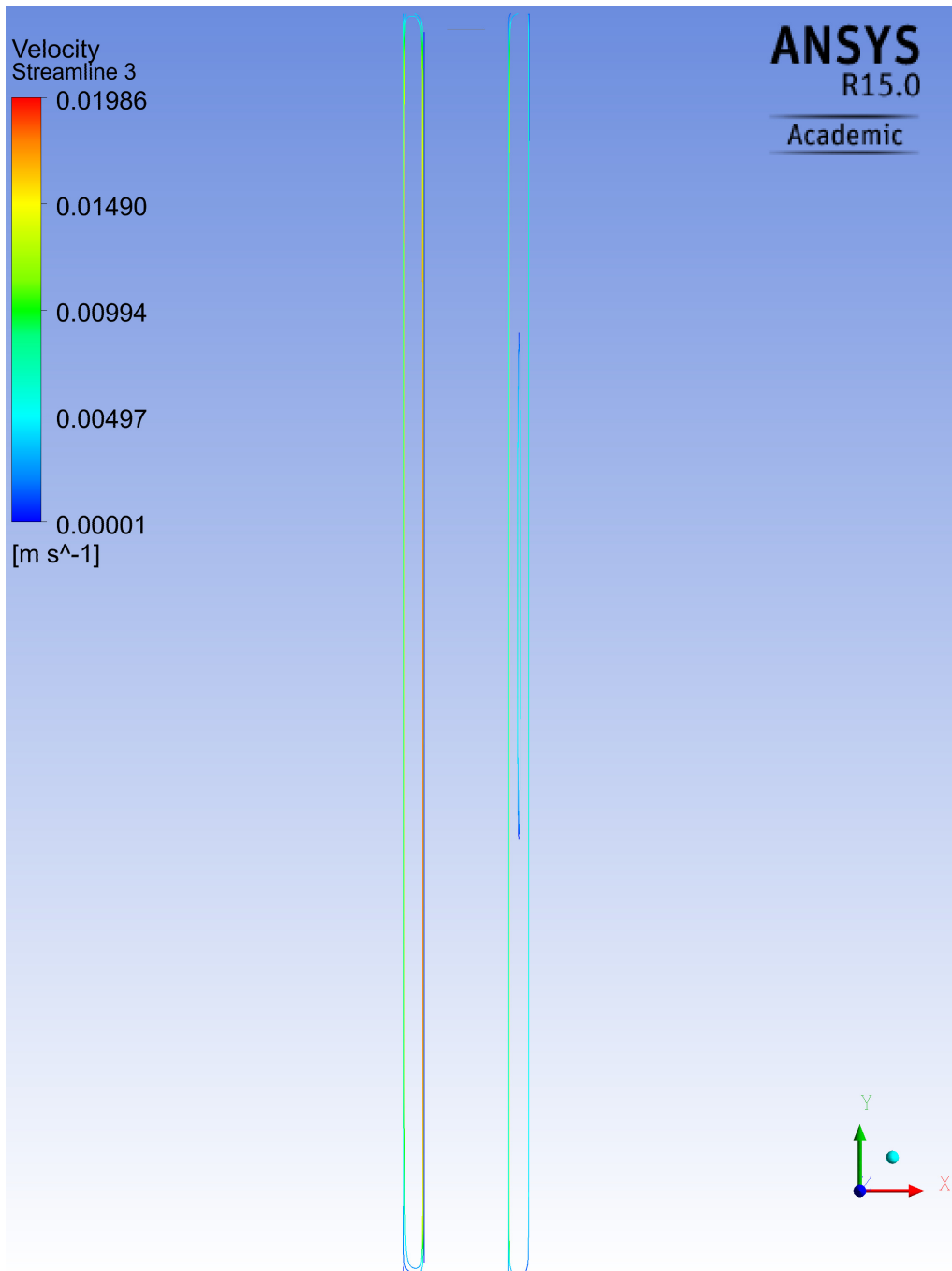
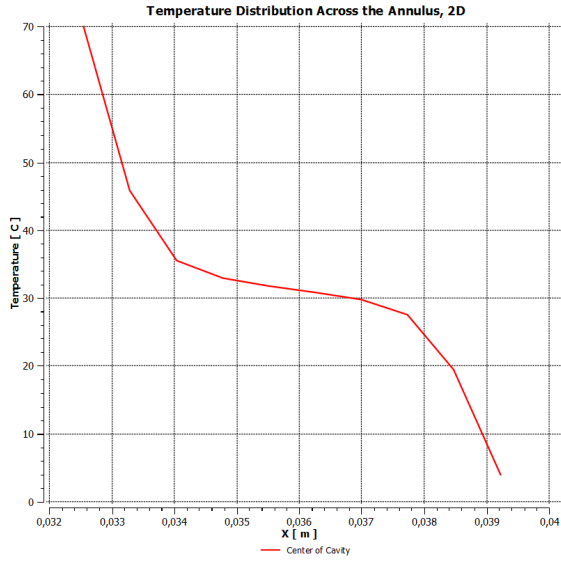
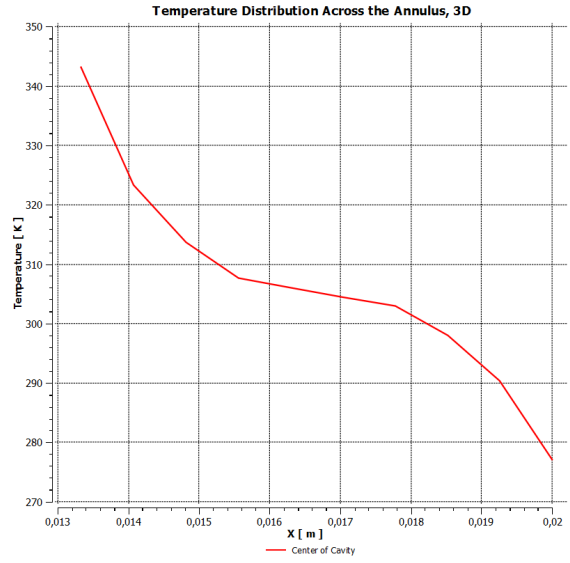


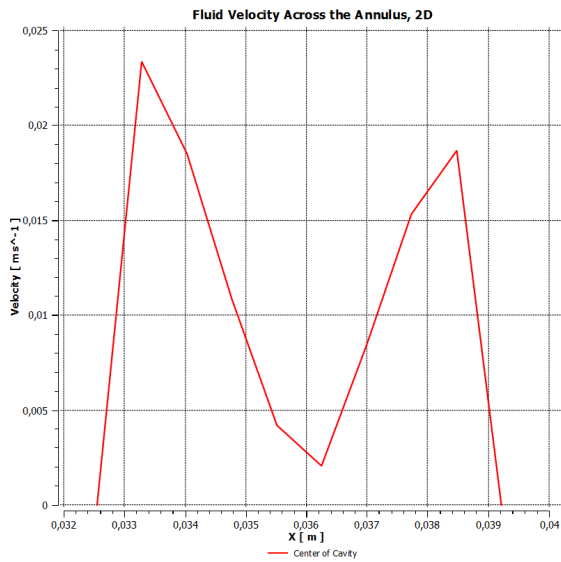
FIGURE 22: Streamlines from the 3D model, showing the circulation occurring in the cavity



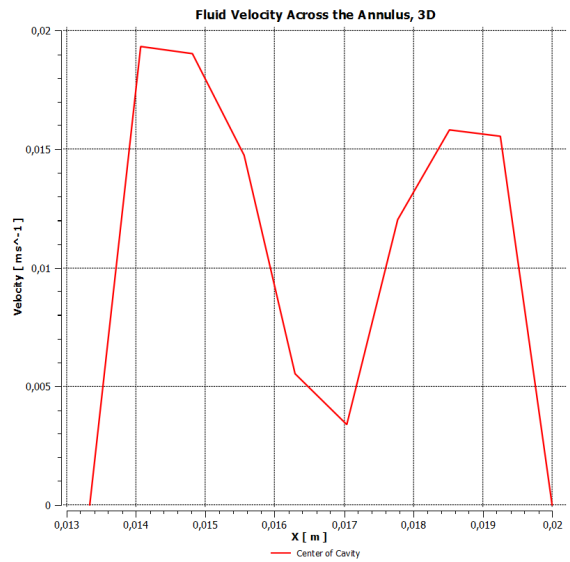
(A) Temperature distribution across the annulus, 2D



(B) Temperature distribution across the annulus, 3D



(C) Velocity distribution across the annulus, 2D



(D) Velocity distribution across the annulus, 3D

FIGURE 23: Temperature and velocity distribution in the center of the cavity of the 2D and 3D models

Figure 23 presents the temperature and velocity distribution in the natural convection 2D and 3D models when the inner cylinder wall is at a temperature of 70°C . It can be seen from Figure 23a and 23b that the temperature distribution predicted by the 2D model is close to the predictions of the 3D model. The core of the cylinder holds a temperature of approximately 30°C ($\sim 305\text{ K}$).

Figure 23c and 23d shows that the velocity across the annulus of the cavity is not symmetrical, but reaches a higher value closer to the inner wall compared to the outer

walls. It can also be seen that midway across the annulus, the fluid velocity is close to stagnant. The different shapes of the 2D and 3D graphs implies that the temperatures distribution is more even in the concentric cylinder than in the wedge.

Figure 24 shows the direction of the fluid movement in the center of the cavity. It can be seen that the fluid closest to the hot wall moves with a higher velocity than the rest of the fluid, whereas the fluid closest to the outer wall has a moderate speed relative to the highest velocity occurring in the cavity. The behavior of boundary layer type flow and heat transfer is apparent because both temperature and velocity gradients peak near the heated and cooled wall. The low gradients of temperature and velocity in the middle of the enclosure further indicate a stagnant and stratified core.

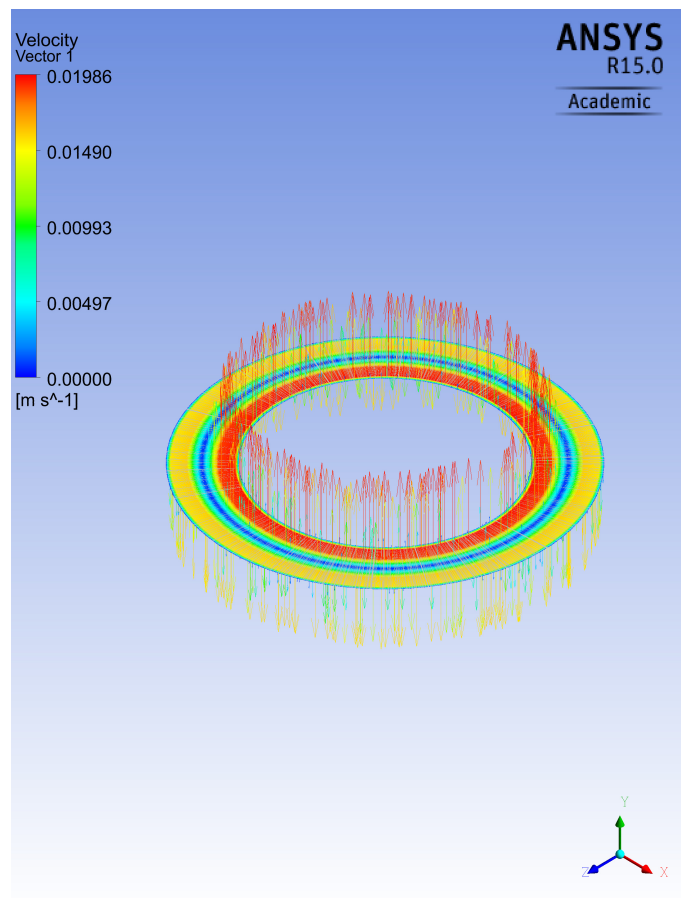
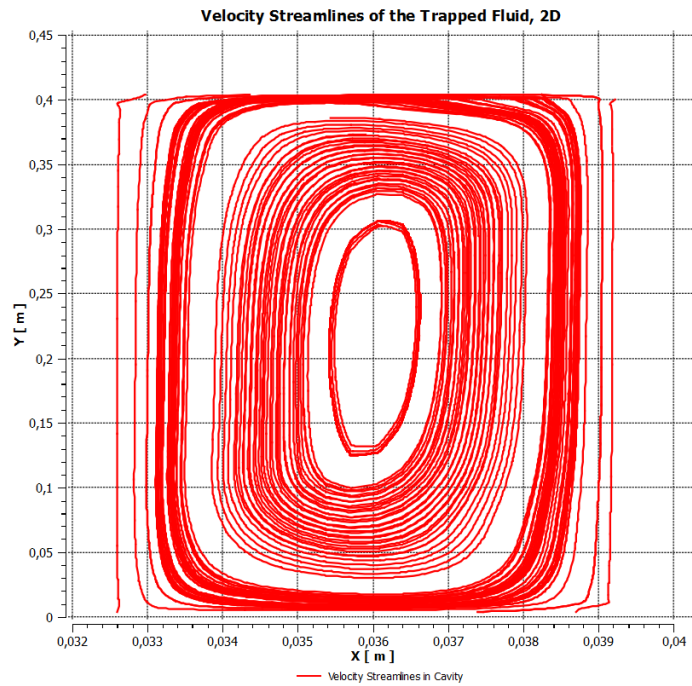
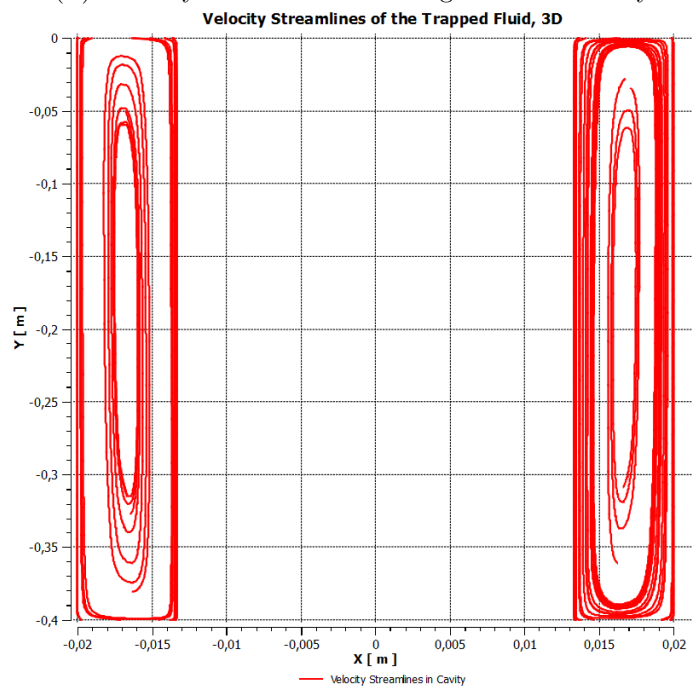


FIGURE 24: Behaviour of the fluid velocity in the center of the cavity with the inner cylinder wall being $70^{\circ}C$

Figure 25 presents the velocity streamlines occurring in the enclosure, where 25a occurred in the wedge, while 25b is based on values from the cylinder.



(A) Velocity streamlines occurring in the 2D cavity



(B) Velocity streamlines occurring in the 3D cavity

FIGURE 25: Velocity streamlines occurring in the 2D (25a) and 3D (25b) cavities

7 Discussion

Heat transfer values from the simulations were extracted from processing the results from the CFX-Solver Manager in CFD-Post. Mainly the heat flux from the simplified model and the heat transfer coefficient from the fully resolved model were of interest, so that the CFD-results could be compared to the analytical solution. The *Function Calculator* found in CFD-Post was used to calculate heat transfer values such as the heat flux at different locations. The results for the simplified model and fully resolved model for different temperatures, are presented in Table A1, A2, A3 and A4.

Heat flux in CFX is specified across the wall boundary, where a positive value indicates heat flux into the domain and negative values indicate that heat is transferred out of the domain. ANSYS CFX operates with a `Wall Heat Flux` variable and a `Heat Flux` variable. Both of the terms are defined as the total heat flux into the domain, including convective and radiative contributions. The difference between them is that `Heat Flux` can be plotted local to a specific boundary condition without contributions from adjacent boundary conditions as opposed to the `Wall Heat Flux` variable. Another difference is the fact that `Wall Heat Flux` is computed by the CFX-Solver which utilizes an arithmetic averaging procedure, while `Heat Flux` is computed by the post processor directly from the convective energy flows that are written to the results file, and thereby avoids this averaging of the values (ANSYS®, 2013). Based on these definitions, the `Heat Flux` function was preferred and used in extracting information about the trapped fluid volumes investigated in this study.

To find the heat transfer coefficient from the results obtained with the fully resolved model, the heat flux at the inner and outer wall from the simulations were calculated by the area-weighted average function:

$$\text{areaAve}[\text{Heat Flux}]\text{@Location} \quad (44)$$

where the **Location** was either set to **InnerWall** or **OuterWall** as specified in the boundary conditions.

If rearranging Eq (43), one see that the heat transfer coefficient will be quite large when computed by CFX, due to the fact that CFX will use a near-wall temperature as T_{cold} (see Eq. (39) and (43)) instead of the actual delta temperature across the annulus. This will make ΔT quite small and hence h large. To be consistent with the literature, the average heat transfer coefficient was therefore calculated from the following relation:

$$\begin{aligned} Q_A &= \int_A q \, dA = hA(T_{hot} - T_{cold}) \\ \Rightarrow h &= \frac{Q_A}{A(T_{hot} - T_{cold})} \end{aligned} \quad (45)$$

Since the heat flux is defined as watts per meter squared [W/m^2], the heat transfer coefficient was simply computed by taking the heat flux value calculated by the *Function Calculator* in CFD-post, and divide it by the relevant temperature difference.

It was expected that the heat flux at the inner wall would be approximately equal to the heat flux at the outer wall, due to the laws of conservation. This proved however to be wrong for both the simplified model and the fully resolved model, and differences up to approximately 35% were observed for the simplified and fully resolved models. The different values can be seen in Table A1, A2, A3 and A4.

An explanation to this may be that the heat distribution in the cavity is asymmetrical due to the features of natural convection, that is the warmer fluid is located in a region at the top of the cavity close to the inner wall, while a respective cold region is found at the bottom of the cavity, closer to the outer wall. With CFX computing the average heat flux as in Eq. (43), this approach will thus yield different heat fluxes at the inner and outer wall. This does however not explain the heat flux differences that one also find in the simplified model results, where the heat transfer happens through conduction only.

Another explanation that could relate to both the conduction and convection models, is again the way CFX computes the heat flux at the respective walls (Eq. (43)), but in a combination with the different surface areas of the inner and outer wall (see Section 5.1). With the inner wall dealing with higher temperatures as well as having a smaller area to distribute the heat across, compared to the outer wall which deals with lower temperatures as well as having a larger area to disperse the heat over, this may be reflected in the area-weighted heat fluxes occurring at the walls. It is however the delta temperature between the wall temperature and the near-wall temperature that is involved in the calculations, which does not depend on the wall temperature itself. An important factor is therefore how CFX decides on the $T_{cold} = T_{nW}$ temperature, and how big of a gap this constitutes up to the wall temperature.

In the following sections it can be seen that the heat flux extracted from the CFD results for comparison with the values obtained in the analytical solution, are the heat fluxes at the **InnerWall** of the model. An average value between the heat fluxes could possibly have been used, but as the heat flux at the inner wall was higher than the one at the outer wall, it was decided that safer predictions would be made if conclusions were based on these values. Another aspect playing part is the fact that the heat at the inner wall will have to go somewhere due to fluid motion, which would have to be towards colder environs due to the laws of heat transfer. Since the upper and lower boundaries of the cavity were insulated, the only escaping route would be through the outer wall. Although this area was larger, the same amount of heat coming from the inner wall would still hit the outer wall.

7.1 2D vs 3D

From Figure 26 one can observe that there is almost no difference between the 2D and the 3D models when the heat transfer occurs through conduction and the same boundary conditions apply to both models. The 2D model is presented in black, but is barely spottable behind the red 3D graphs. This agreement between the 2D and 3D models might be expected, following from the Fourier's Law (Eq. (1)), which implies that the heat transfer through conduction only depends on a material's thermal conductivity, a temperature gradient and a distance over which the heat is transported. In this case, the distance would be the length of the annular gap, which is the same for both models. The differences that however are present may be due to 2D and 3D grid differences seen in Section 5.3.

It can be discussed if the models are comparable if the grid densities are unequal to each other. Table 9 shows that the temperatures predicted by Grid 3 only differ with 0.32% up to Grid 5, indicating almost the same temperature predictions by both models when the higher wall temperature is 70°C. Although the monitored temperatures were measured at different points due to the geometries being modeled at different places in the DesignModeler-space, they are equivalent to each other (that is in the middle of the center of the cavity). Since the temperatures are close to similar, it is reasonable to believe that the 2D and 3D models are comparable, despite the grid density differences.

An effective thermal conductivity based on the Nusselt number from the Wärmearbeitsatlas (2006) correlation, predicts a heat flux of approximately 40-100 kW/m² at the inner wall of the concentric cylinder for temperatures between 50-100°C. The three other correlations follows shortly after and predict values closer to each other, with minimum values ranging from approximately 28-31 kW/m² to maximum values around 70-88 kW/m².

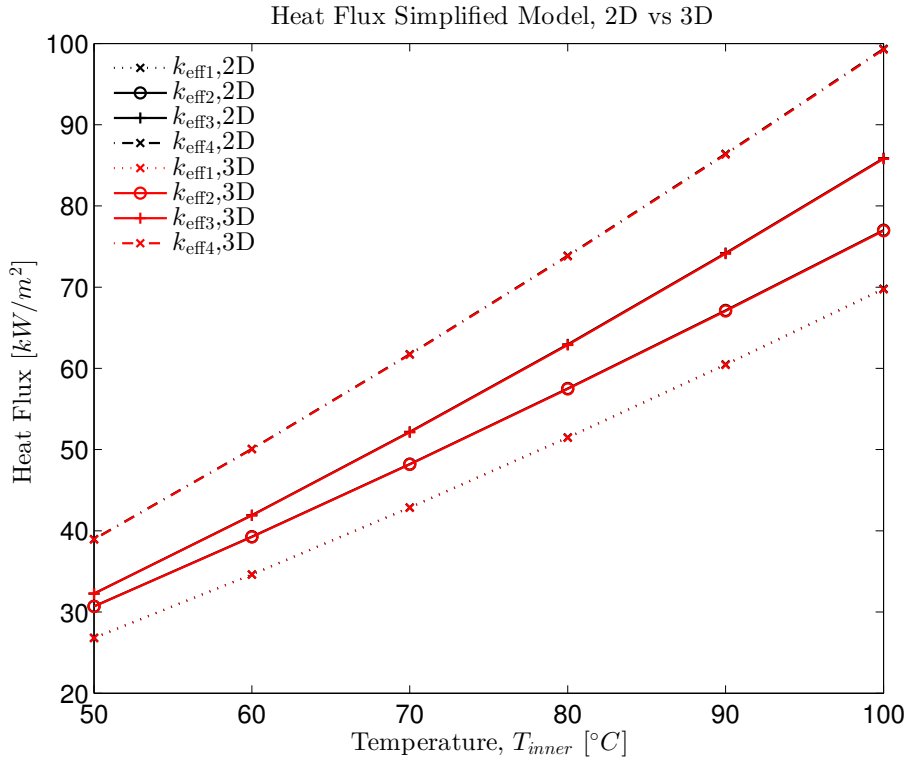
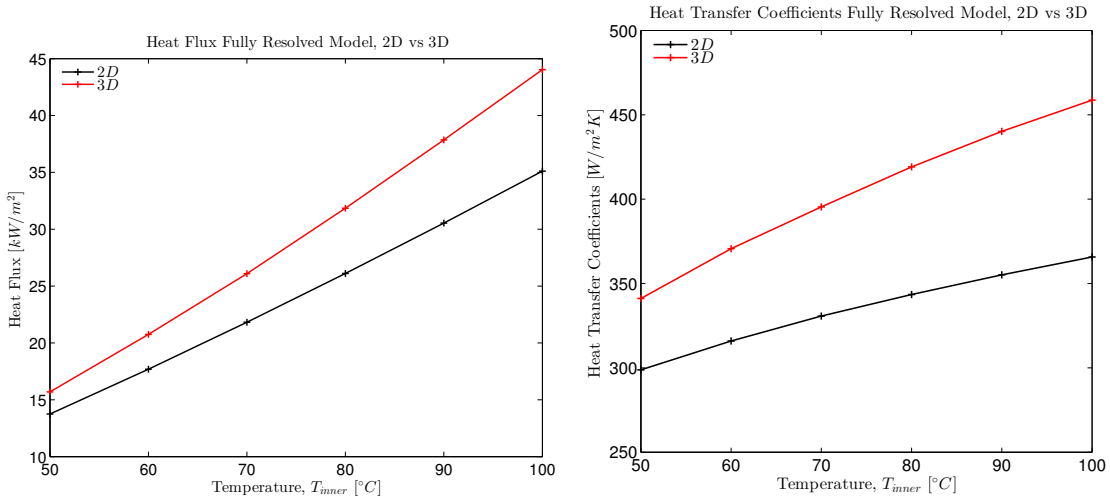


FIGURE 26: Comparison of the heat flux appearing in the simplified 2D and 3D models

The fully resolved 2D and 3D models predict greater differences between each other compared to the simplified models, and can be seen in Figure 27. The 3D fully resolved model predicts greater heat flux values than the 2D fully resolved model. An explanation to this might be that the 3D model is able to capture the flow better. Free-convective heat transfer depends strongly on the geometry as discussed earlier, and the turbulent fluctuations may be influenced by being trapped in an annulus compared to a one-element thick 2D wedge. Additionally, the grid differences will also be of significance here as for the simplified model. Normally the amount of mesh elements is equivalent to the accuracy of the heat transfer predictions, and can be of great importance in predicting the tiny turbulent fluctuations playing a vigorous part in the convective heat transfer.



(A) Comparison of the heat flux appearing in the 2D and 3D fully resolved models
 (B) Comparison of the heat transfer coefficient appearing in the 2D and 3D fully resolved models

FIGURE 27: Comparison of the 2D and 3D fully resolved models

Figure 27a shows that when accounting for the free convection effects and not assuming a uniform thermal behaviour throughout the annulus, heat fluxes of approximately 15-45 kW/m^2 is presented, with respective heat transfer coefficients of 300-450 W/m^2K (Figure 27b). It can then be seen that the minimum heat flux value the simplified model predicts, is almost equal to the maximum heat flux value the fully resolved model predicts, implying major differences.

A difference of up to 22% could be seen between the 2D and 3D fully resolved models, where the 3D model values exceeded the 2D model values for every delta temperature tested.

7.2 Simplified Model vs Fully Resolved Model

Because the simplified model predicted considerably similar results for the 2D and 3D model, the results obtained with the 3D conduction model were used for further comparison because it predicted fairly larger heat flux than the 2D model. Basing predictions upon the greater values were thought to give safer computation estimates with respect to protection of subsea equipment.

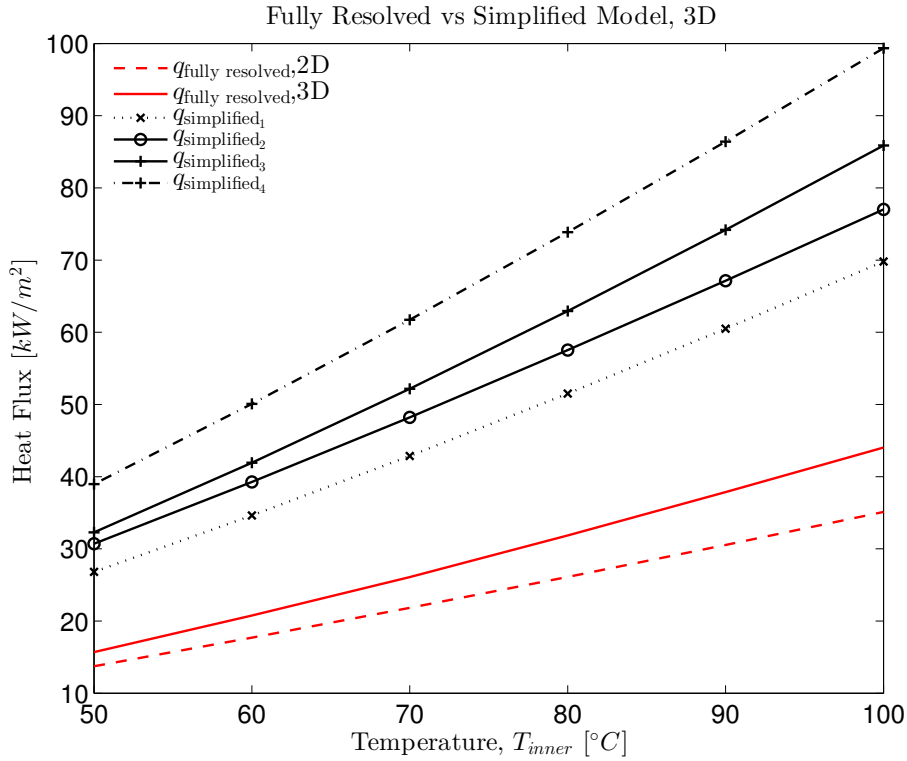


FIGURE 28: Comparison of the fully resolved 2D and 3D models with the simplified 3D model

From Figure 28 one can observe that the thermal analysis of the fully resolved model predicts a considerably lower heat flux than the simplified model based on the effective thermal conductivities from Section 5.2.1. The fact that the conduction model predicts values exceeding the fully resolved model with approximately 65% at the most, indicates that if the simplified model is used in subsea computations, it may overestimate the heat loss actual occurring. This is not necessarily a drawback, as overestimating heat losses will be preferred over underestimating them. It is rather a question about to what degree one would like to overestimate the losses to be on the safe side when it comes to equipment protection and insulation, as this also has a cost.

Between the values of the fully resolved 3D model, and the lower values of the predicted heat flux by the correlations, that is $q_{\text{simplified}_1}$ from Eq. (32), differences up to approximately 40 % can be found.

7.3 Analytical Solution vs Fully Resolved Model

Figure 29 shows that based on the conditions applying to this study, the fully resolved model predicts that more heat is transferred in the cavity as the temperature difference increases compared to the predictions of the correlations. Between the fully resolved 3D model and correlation equation (36) from VDI-Wärmeatlas (2006), a difference of

approximately 12% at the most is seen in the heat transfer coefficient predictions. This is the lowest deviation present between the analytical solutions and the fully resolved CFD-solution. The three correlations from Eq. (32), (34) and (35) all predict lower heat transfer coefficients than the fully resolved 2D and 3D models, although the correlation from Eq. (35) predicts heat transfer coefficient values fairly close to the 2D fully resolved model.

As mentioned in Section 4, it is expected that the heat transfer coefficient increases with increasing temperatures. Higher temperatures in the cavity will result in more unstable temperature gradients, and the buoyancy forces will transfer warmer fluid upwards. The warmer fluid will after a time come in contact with colder fluid and become more dense as the fluid temperature decreases. The gravity forces on the fluid will then become larger than the buoyancy forces, and fluid is transferred downwards in the cavity. Higher temperatures will therefore normally result in more fluid motion and hence higher heat transfer rates. This will impact the heat transfer coefficient which is dependent upon the amount of heat transferred.

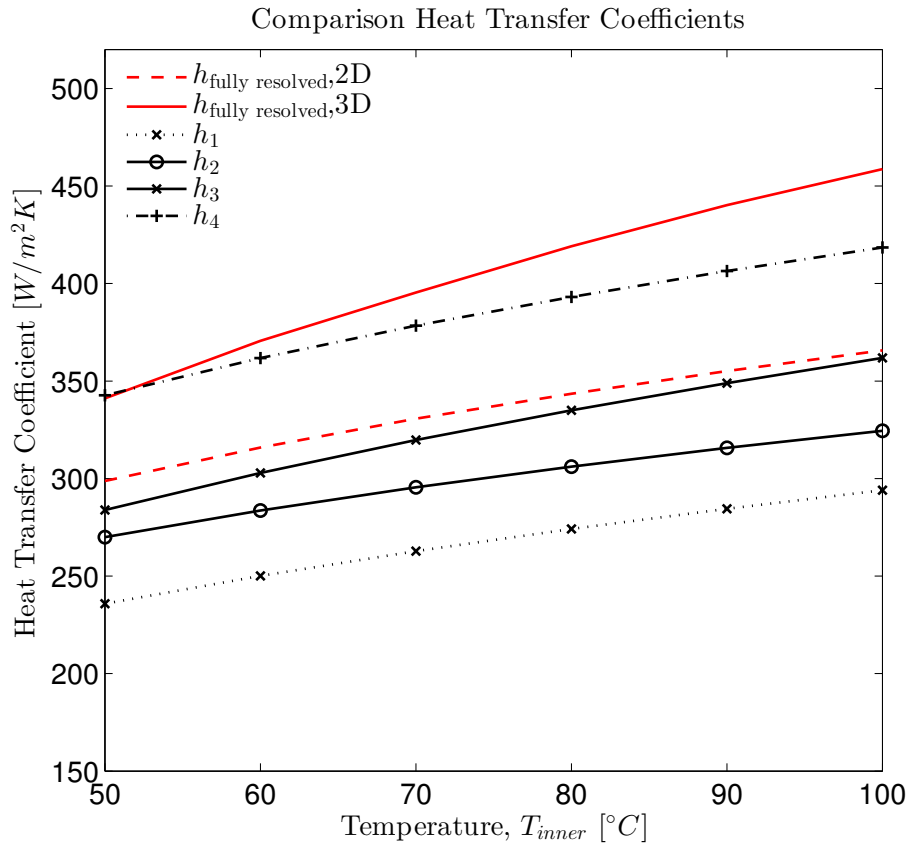


FIGURE 29: Comparison of the analytical heat transfer coefficient and the heat transfer coefficient obtained with the 2D and 3D fully resolved models

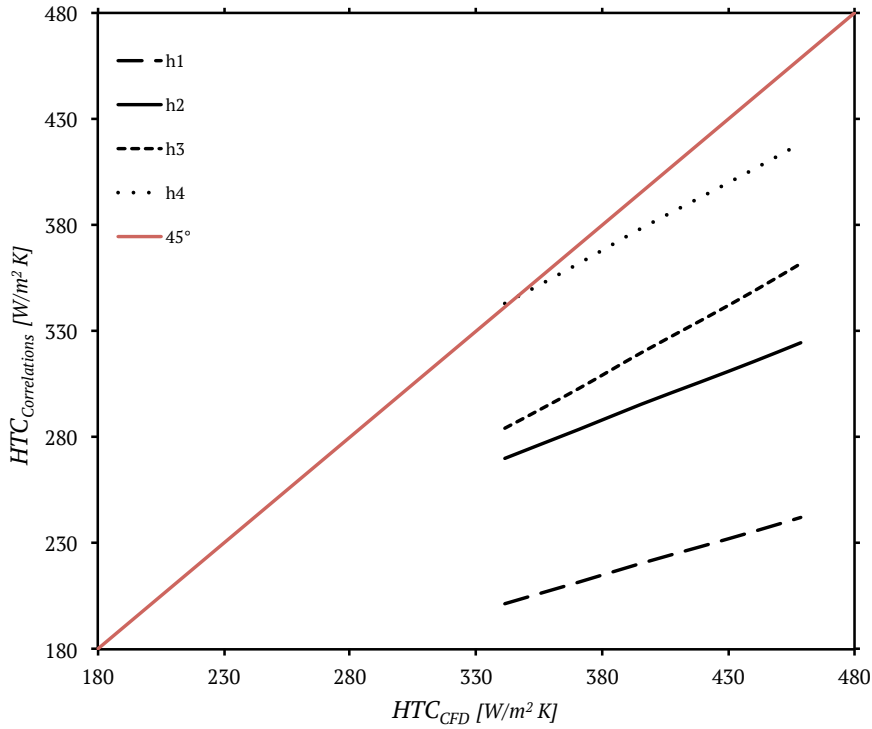


FIGURE 30: Comparison of the heat transfer coefficients found in the analytical solution versus the heat transfer coefficient found with the 3D fully resolved model in ANSYS CFX. The red line represents the case where the values are equal

Figure 30 presents the heat transfer coefficients from the correlations versus the heat transfer coefficient resulting from the fully resolved 3D model, based on inner wall temperatures of 50°C-100°C. The 45° red reference line represents the case where the heat transfer coefficients are equal to each other. One can observe that h_4 , that is the heat transfer coefficient based on the correlation from VDI-Wärmeatlas, lies closer to the reference line than the three other correlations. This implies that the heat transfer coefficient estimated by Eq. (36) is close to the heat transfer coefficient estimated by the computational analysis of free convection.

7.4 Analytic Solution vs Simplified Model vs Fully Resolved Model

Figure 31 gather all the results from the analytical solution, the simplified model and the fully resolved model. As discussed, there is a gap between the simplified model graphs and the graphs from the two other models. This gap is caused by the effective thermal conductivity computed by the Nusselt number equations from the four correlations Eq. (32), (34), (35) and (36) and the assumption about heat transfer occurring through conduction. It can be argued that this difference in heat loss estimations ensures safer predictions regarding subsea equipment, and is therefore seen as necessary. It may be reasonable to

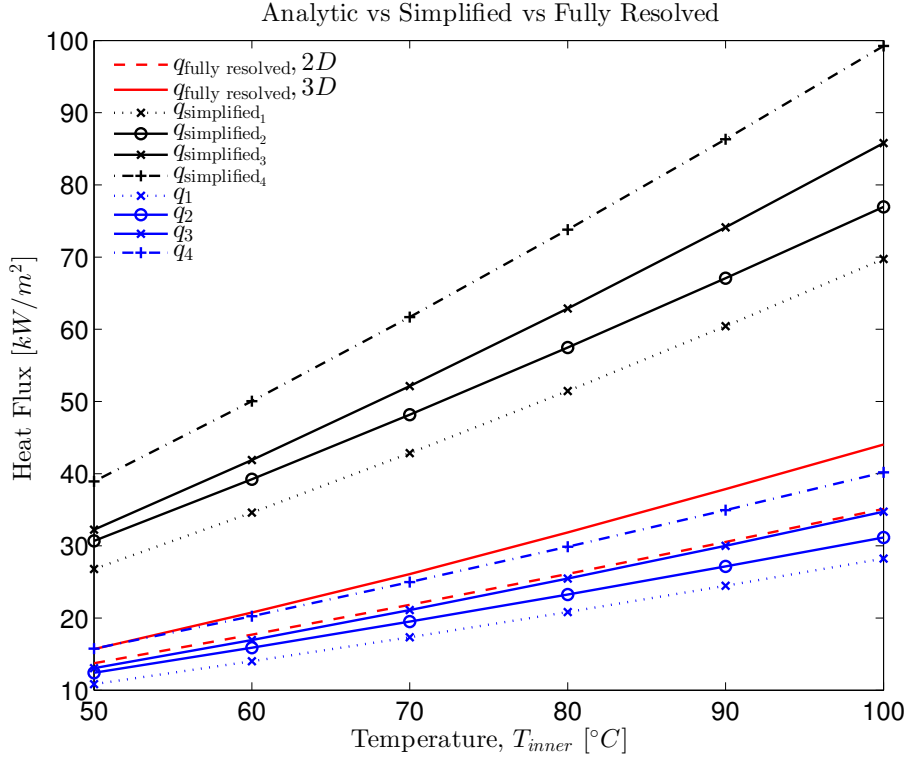


FIGURE 31: Comparison between the heat flux values obtained from the analytical solution, the simplified 3D model and the fully resolved 2D and 3D models

assume that expenses related to insulation and protection material corresponding to heat losses of 100 kW/m^2 could be halved if the assumed heat loss is reduced to 50 kW/m^2 . In this case, with the characteristic dimensions as in Table 2, it would be sufficient to account for heat losses of 50 kW/m^2 through the cavity according to the CFD results. A predicted value of 50 kW/m^2 would in this case give a margin of approximately 6 kW/m^2 down to the actual predicted CFD value, and could probably be sufficient as a security buffer.

These results are however only based on one specific cavity. With different geometries comes different heat losses. If every cavity is assumed to lose heat close to 50 kW/m^2 , it is reasonable to believe that some of the costs related to insulation may be reduced, if the correlation from Eq. (36) is used as a basis for the simplified model and large delta temperatures are dealt with. If many of the cavities are neglected in computations related to insulation and material protection however, an estimated heat loss of 100 kW/m^2 may be reasonable.

A simplified heat transfer model will in many cases ensure that insulation and protection materials are adequate in accordance with the conditions the relevant equipment is located in. Another advantage with the simplified model is that it is effective and cheap. The industry is also experienced with this method, so one know that the production will

function if the heat losses are accounted for in this way.

CFD simulations are on the other hand more time-consuming and expensive. Although numerical predictions may be more accurate, it could be that the extra time spent on CFD is worth the extra cost relative to overestimating heat losses.

7.5 Verification and Validation

An important part of CFD-analyses is to verify whether the solutions are valid or not. Numerical experiments are vulnerable to uncertainties and errors such as assumptions, simplifications and limitations.

Errors in CFD solutions may be classified as either acknowledged errors or unacknowledged errors. Acknowledged errors are typically physical approximation errors, round-off errors, convergence errors or discretization errors that there are procedures for identifying, and possibly removing. Unacknowledged errors on the other hand, are user errors or computer programming errors within the program, which there are no procedures for finding. Uncertainties indicate that deficiencies may or may not exist (Slater, 2008).

It is reasonable to believe that one of the largest errors in the CFD simulations will be due to physical approximation errors arising from the geometries used. The geometries, a one-element thick wedge (2D), and a simple concentric cylinder (3D) were not complex in itself, but the actual geometries containing trapped fluid volumes in subsea christmas trees are believed to be more complicated and compounded. If several steel structures are located close to each other and each contain trapped fluids at different temperatures with different heat transfer properties, the heat transfer will be a combination of conduction and convection, which might influence the heat loss out of the christmas tree and into the sea. This study was based on only one geometry type and one characteristic length between the inner and outer wall. The results can therefore not be generalized or interpreted as applicable to all trapped fluids in subsea christmas tree enclosures. It is however indicative of the fluid behaviour that will occur in a concentric cylinder due to the increasing temperature differences and free convection effects.

The CFD results will also be affected by the fluid properties the simulations are run with. Pure water was utilized in this study, although a mix of saline water and glycols are common to find in subsea christmas trees cavities. Saline water will according to the findings in (Pantokratoras, 2000) affect the fluid properties, which in turn will impact the heat transfer abilities. It is also known that glycols, as for instance monoethylene glycol (MEG), changes the fluid properties and hence the heat transfer behaviour. The amount of water in the enclosures may also influence the simulations. In this case a full cavity was investigated, but it is likely that less fluid would impact the rate of heat transferred across the annulus, depending on what substances and material properties the rest of the cavity consists of.

Due to very low velocities, it is reasonable to believe there might be a round-off error

in the computations. It is believed these are quite small, since CFX was able to capture the free convection effects occurring in the enclosure, as seen in Section 6.2. The number of iterations can influence the results tremendously, but due to the grid independence study in Section 5.7 it was believed the numerical results from CFX were trustworthy. The number of iterations could have been raised, but was due to time constraints kept at a constant number of 2000 iterations to be consistent with the different temperature runs.

For the 3D model, it was seen that more than 4000 iterations were needed to get the total domain imbalances down to a level of 0. The heat flux at the inner wall of the cylinder was then increased with approximately 0.1 kW/m^2 . Based on this, it is believed that if the number of iterations were doubled for every simulation performed, the heat flux estimations would have experienced an average increase of 0.1 kW/m^2 . Taking this into account, the predicted heat losses will be even higher compared to the analytical solutions, but still below the results obtained with the effective thermal conductivity.

The boundary conditions will influence the results to a great extent, together with the wall roughness in the cavity. The correlations, except Eq. (36), were not perfect matches with the geometry and numerical setup used in the development of the free convection model in this study. Two of them were based on rectangular boxes, while one of them on an open-ended concentric cylinder. Some of the correlations were even established based on laminar flow. This may be an explanation to why three of the correlations predict lower heat transfer values compared to the fully resolved 3D model. Why Eq. (36) predicts lower heat transfer values than the CFD-results when T_{hot} increases above 50°C , may be due to different experiment conditions.

The solution may be exposed to discretization errors due to the grid density and timestep chosen. This was however tested in Section 5.7, where a fine 2D mesh and a medium 3D mesh were concluded as sufficient. A physical timestep of 0.01 seconds was used for faster convergence. By using the finest grid for the 3D model, it is possible that more accurate results would have been obtained since the solution changes from Grid 5 to Grid 6 as seen in Table 9. A dramatically improved accuracy is however not expected, as the temperature change from Grid 5 to 6 is only predicted to be 0.23%.

It was later discovered that solving the problem in double precision instead of single precision could be beneficial relative to the accuracy of the solutions, due to the complicated behaviour of natural convection.

To get an approximate error band of the numerical solution, a measure of the percentage a computed solution deviates from the value of the asymptotic numerical value called *Grid Convergence Index* (**GCI**) can be computed. According to Slater (2008), this

is given by

$$\mathbf{GCI}_{fine} = \frac{F_s |\varepsilon|}{(r^p - 1)} \quad (46)$$

$$\mathbf{GCI}_{coarse} = \frac{F_s |\varepsilon| r^p}{(r^p - 1)}, \quad (47)$$

depending on whether one uses the fine mesh (\mathbf{GCI}_{fine}) or the coarser mesh (\mathbf{GCI}_{coarse}). Here, F_s is a factor of safety, $r = h_2/h_1$ is the grid refinement ratio, with h_1 being a finer grid spacing than h_2 , and p is the order of grid convergence. The relative error is defined by Slater (2008) as

$$\varepsilon = \frac{f_2 - f_1}{f_1},$$

where f_1 is a quantity of interest resulting from a simulation executed with the finer grid, and f_2 with a coarser grid.

A safety factor of 1.25 was suggested by Slater (2008) for comparison of two grids, and a theoretical order of convergence $p = 2$ was utilized for the grid computations. The \mathbf{GCI} s for the grids presented in Table 9, can be seen in Table 10.

Since Grid 5 was preferred over Grid 6, it can be expected from Eq. (47) that the 3D model will have an error band of $\sim 0.95\%$. The finest 2D model, that is Grid 3, was used in this study, and hence Eq. (46) predicts an error band of 0.00824%.

| Grid | 1-2 | 2-3 | 4-5 | 5-6 |
|-----------------|----------|----------|----------|----------|
| p | 2 | 2 | 2 | 2 |
| F_s | 1.25 | 1.25 | 1.25 | 1.25 |
| $ \varepsilon $ | 2.63E-04 | 9.86E-05 | 4.16E-03 | 2.32E-03 |
| r | 1.5 | 1.58 | 2.0 | 1.20 |
| \mathbf{GCI} | 2.63E-04 | 8.24E-05 | 1.73E-03 | 6.59E-03 |

TABLE 10: Grid convergence index

ANSYS CFX is a huge and complex program, and it takes time to familiarize with all the functions and features it has to offer. There might be functions that could have improved the results, but which have not been exploited by the user due to unawareness of them. ANSYS-files require a lot of disk memory, and several problems were related to this. If data was lost or hurt in processes where ANSYS loaded or saved files, it is possible that this could have affected the simulations. A work station may be recommended for better performance and handling of the data.

8 Conclusions

Simplifications regarding thermal behaviour in subsea christmas trees and other equipment are common to utilize in heat transfer computations and estimations. Free-convective heat transfer in cavities is very often assumed to behave as a solid body with an effective thermal conductivity, or sometimes even neglected. Subsea christmas trees are complex in nature, containing several cavities which all make contributions to the overall heat loss if not accounted for and insulated. Insulation is important in maintaining and possibly improve flow performance, as well as retaining latent heat when production is interrupted, otherwise temperatures may fall and hydrates form under the high operating pressures that are present. Hydrates may cause blockage of the well stream and will have to be removed which is an extensive process in time, cost and risk.

The analytical solution based on literature correlations predicted less heat transfer occurring in the cavity compared to what the 3D model did, which took into account the free convection effects. The correlations based on rectangular enclosures proved to predict the lowest heat flux values, and estimated heat fluxes between approximately 11-31 kW/m². The correlation for an open-ended concentric cylinder, Eq. (35), predicted values close to the rectangular enclosures, but reached a maximum value of 35 kW/m² when the inner wall temperature was 100°C and the sea water was 4°C. Eq. (36) from VDI-Wärmeatlas (2006), which was valid for closed concentric cylinders heated from the inside to the outside, predicted heat flux values of approximately 16-40 kW/m² in the temperature range 50-100°C. The latter correlation was in closest relation to the fully resolved 3D model, which from the thermal CFD-analysis predicted heat fluxes of approximately 16-45 kW/m² for the same temperature range, resulting in deviations up to 11% related to the VDI-Wärmeatlas-correlation.

The 2D fully resolved model predicted heat fluxes between 14-35 kW/m², which proved to be very close to the predictions of the open-ended cylinder correlation according to Eq. (35). It underestimated the heat flux values with a 12-23% error, depending on the temperature of the inner wall. The error was seen increasing with increasing temperatures, and it is likely to conclude that a 2D fully resolved model is inadequate for heat transfer calculations of concentric cylinder enclosures.

The effective thermal conductivities that were estimated based on the Nusselt number obtained from the literature correlations and the thermal conductivity of water, indicated that heat fluxes in the vertical circular enclosure would go from a minimum of 30 kW/m² for 50°C to a maximum of 100 kW/m² for 100°C. This implies that when assuming the free convection effects in trapped fluid cavities behave as a solid with temperature-independent properties, one may be overestimating the heat losses with 47-60% according to this investigation. If neglecting some of the trapped fluid cavities in subsea christmas tree computations, this overestimate may be reasonable depending on the geometry and number of

cavities. An overestimate could also possibly ensure reliable production. The effort that would have to be put down into doing a proper CFD analysis may exceed the cost of overestimating heat losses in terms of time and insulation material, given that all christmas trees need to be individually analysed. If individual analyses are not required, current technology might be sufficient.

The free convection model and heat transfer results developed in this study can only be seen as an indication to the heat losses occurring in trapped fluid volumes inside subsea christmas trees, more than an accurate representation of the real world.

It might however encourage to further investigation with more complicated geometries since contributions of various trapped fluids are neglected in the conventional FEA approach and a CFD analysis could predict a more realistic thermal behaviour by including the cavity volumes, hence there could be a financial upside running more extensive simulations.

References

- ANSYS®(2013), *Help Viewer*, Academic Research, Release 15.0, ANSYS, Inc.
- Bejan, A. (2013), *Internal Natural Convection*, 4th edition edn, John Wiley & Sons, Inc., pp. 233–294.
URL: <http://dx.doi.org/10.1002/9781118671627.ch5>
- Burmeister, C. (1993), *Convective Heat Transfer*, John Wiley & Sons, chapter 10.
- Deutscher, I. V. (2006), Wärmeübergang durch freie konvektion in geschlossenen fluidschichten, in H. Klan, ed., ‘VDI-Wärmeatlas: Berechnungsblätter Für Den Wärmeübergang’, VDI Buch, Springer Verlag, Dusseldorf, chapter 7, pp. 24–26.
- Faghri, A., Zhang, Y. and Howell, J. (2010), *Advanced Heat and Mass Transfer*, Global Digital Press, chapter 6 Natural Convection.
- Hadjadj, A., Maamir, S. and Zeghmami, B. (1999), ‘A new study of laminar natural convection in two concentric vertical cylinders’, pp. 113–121.
URL: <http://dx.doi.org/10.1007/s002310050304>
- Incropera, DeWitt, Bergman and Lavine (2007), *Fundamentals of Heat and Mass Transfer*, sixth edn, John Wiley & Sons, chapter 9.
- Jiji, L. M. (2009), *Heat Convection*, second edn, Springer.
- Lu, Y., Marotta, E. and Skeels, H. B. (2011), Cfd thermal analysis of subsea equipment and experimental validation, number OTC 21553, Offshore Technology Conference, Houston, Texas, USA.
- Martynenko, O. G. and Khramtsov, P. P. (2005), Natural convection in enclosures, in ‘Free-Convective Heat Transfer’, Springer Berlin Heidelberg, pp. 279–343.
- MathWorks®(2013), ‘Matlab’.
URL: <http://www.mathworks.se/products/matlab/>
- Pantokratoras, A. (2000), ‘Laminar natural convection of pure and a vertical isothermal cylinder saline water along’, **36**(4), 351–360.
URL: <http://dx.doi.org/10.1007/s002310000072>
- Rohsenow, W., Hartnett, J. and Cho, Y. I. (1998), *Handbook of Heat Transfer*, 3rd edition edn, McGraw-Hill Education.
- Sachdeva, C. (2009), *Fundamentals of Engineering Heat and Mass Transfer*, New Age Science, chapter 8.

Slater, J. W. (2008), 'Examining spatial (grid) convergence'.

URL: <http://www.grc.nasa.gov/WWW/wind/valid/tutorial/spatconv.html>

Smith, R. (2009), Heat conduction and the heat equation. http://www4.ncsu.edu/~rsmith/MA573_F09/Heat_Equation.pdf.

Versteeg, H. K. and Malalasekera, W. (1995), *Computational Fluid Dynamics: The Finite Volume Method*, 2nd edition edn, Pearson Education Limited 1995, 2007, chapter 5, pp. 134–178.

A Simplified Model Results

| @InnerWall | | | | | |
|------------------|---------------------------|---------------------------|---------------|------------|------------|
| k_{eff} | 2D | 3D | Deviation [%] | T_i [°C] | ΔT |
| | q'' [W/m ²] | q'' [W/m ²] | | | |
| 3.144 | 26789.1 | 26816.6 | 0.10 | | |
| 3.600 | 30674.4 | 30705.8 | 0.10 | 50 | 46 |
| 3.785 | 32248.1 | 32281.7 | 0.10 | | |
| 4.569 | 38930.6 | 38972.1 | 0.10 | | |
| 3.335 | 34593.8 | 34629.4 | 0.10 | | |
| 3.782 | 39230.9 | 39271.0 | 0.10 | 60 | 56 |
| 4.039 | 41891.7 | 41934.6 | 0.10 | | |
| 4.824 | 50039.5 | 50090.2 | 0.10 | | |
| 3.504 | 42837.6 | 42869.1 | 0.07 | | |
| 3.940 | 48167.6 | 48203.6 | 0.07 | 70 | 66 |
| 4.264 | 52122.6 | 52176.5 | 0.01 | | |
| 5.046 | 61689.0 | 61734.7 | 0.07 | | |
| 3.655 | 51453.8 | 51506.5 | 0.10 | | |
| 4.082 | 57465.3 | 57523.5 | 0.10 | 80 | 76 |
| 4.467 | 62880.8 | 62944.0 | 0.10 | | |
| 5.242 | 73794.7 | 73870.7 | 0.10 | | |
| 3.793 | 60422.2 | 60483.9 | 0.10 | | |
| 4.210 | 67065.5 | 67133.2 | 0.10 | 90 | 86 |
| 4.6523 | 74117.6 | 74193.2 | 0.10 | | |
| 5.419 | 86324.2 | 86412.7 | 0.10 | | |
| 3.921 | 69724.4 | 69795.6 | 0.10 | | |
| 4.327 | 76943.8 | 77022.7 | 0.10 | 100 | 96 |
| 4.825 | 85792.1 | 85879.8 | 0.10 | | |
| 5.581 | 99243.1 | 99343.7 | 0.10 | | |

TABLE A1: Heat flux at the inner cylinder wall of the simplified model

| @OuterWall | | | | | |
|-------------------|---------------------------|---------------------------|---------------|------------|------------|
| k_{eff} | 2D | 3D | Deviation [%] | T_i [°C] | ΔT |
| | q'' [W/m ²] | q'' [W/m ²] | | | |
| 3.144 | -18045.1 | -17837.1 | 1.2 | | |
| 3.600 | -20662.0 | -20424.0 | 1.2 | 50 | 46 |
| 3.785 | -21722.1 | -21472.1 | 1.2 | | |
| 4.569 | -26223.6 | -25921.4 | 1.2 | | |
| 3.335 | -23302.3 | -23034.0 | 1.2 | | |
| 3.782 | -26425.7 | -26121.1 | 1.2 | 60 | 56 |
| 4.039 | -28217.4 | -27892.4 | 1.2 | | |
| 4.824 | -33705.8 | -33317.8 | 1.2 | | |
| 3.504 | -28854.9 | -28514.5 | 1.2 | | |
| 3.940 | -32445.3 | -32062.7 | 1.2 | 70 | 66 |
| 4.264 | -35109.4 | -34704.8 | 1.2 | | |
| 5.046 | -41552.9 | -41062.9 | 1.2 | | |
| 3.655 | -34658.8 | -34259.7 | 1.2 | | |
| 4.082 | -38707.8 | -38262.2 | 1.0 | 80 | 76 |
| 4.467 | -42356.3 | -41868.0 | 1.2 | | |
| 5.242 | -49706.9 | -49135.1 | 1.0 | | |
| 3.793 | -40700.2 | -40231.1 | 1.2 | | |
| 4.210 | -45174.2 | -44654.3 | 1.2 | 90 | 86 |
| 4.653 | -49924.7 | -49349.4 | 1.2 | | |
| 5.419 | -58147.5 | -57477.5 | 1.2 | | |
| 3.921 | -46965.6 | -46424.9 | 1.2 | | |
| 4.327 | -51829.0 | -51231.8 | 1.2 | 100 | 96 |
| 4.825 | -57788.8 | -57123.7 | 1.2 | | |
| 5.581 | -66848.9 | -66079.5 | 1.2 | | |

TABLE A2: Heat flux at the outer cylinder wall of the simplified model

B Fully Resolved Model Results

| @InnerWall | | | | | | |
|---------------------------|--------------------------|---------------------------|--------------------------|---------------|------------|------------|
| 2D | | 3D | | Deviation [%] | T_i [°C] | ΔT |
| q'' [W/m ²] | h [W/m ² K] | q'' [W/m ²] | h [W/m ² K] | | | |
| 13745.4 | 298.8 | 15690.9 | 341.1 | 12.4 | 50 | 46 |
| 17688.4 | 315.9 | 20755.0 | 370.6 | 14.8 | 60 | 56 |
| 21823.0 | 330.7 | 26096.0 | 395.4 | 16.4 | 70 | 66 |
| 26106.2 | 343.5 | 31850.8 | 419.1 | 18.0 | 80 | 76 |
| 30537.7 | 355.1 | 37857.4 | 440.2 | 19.3 | 90 | 86 |
| 35106.0 | 365.7 | 44039.5 | 458.7 | 20.3 | 100 | 96 |

TABLE A3: Heat flux at the inner cylinder wall of the fully resolved model

| @OuterWall | | | | | | |
|---------------------------|--------------------------|---------------------------|--------------------------|---------------|------------|------------|
| 2D | | 3D | | Deviation [%] | T_i [°C] | ΔT |
| q'' [W/m ²] | h [W/m ² K] | q'' [W/m ²] | h [W/m ² K] | | | |
| -8834.2 | 192.0 | -10025.2 | 217.9 | 11.9 | 50 | -46 |
| -11409.5 | 203.7 | -13211.5 | 235.9 | 13.6 | 60 | -56 |
| -14103.3 | 213.7 | -16752.6 | 253.8 | 15.8 | 70 | -66 |
| -16898.9 | 222.4 | -20460.8 | 269.2 | 17.4 | 80 | -76 |
| -19805.6 | 230.3 | -24377.3 | 283.5 | 18.8 | 90 | -86 |
| -22809.2 | 237.6 | -28426.8 | 296.1 | 19.8 | 100 | -96 |

TABLE A4: Heat flux at the outer cylinder wall of the fully resolved model